Seismic cycle recorded in cockade-bearing faults (Col de Teghime, Alpine Corsica)

Simone Masoch[1*], Michele Fondriest[1], Nereo Preto[1], Michele Secco[2,3], Giulio Di Toro[1,4]

1. Dipartimento di Geoscienze, Università degli Studi di Padova, Padua, ITALY

2. Dipartimento di Ingegneria Edile, Civile ed Ambientale (ICEA), Università degli Studi di Padova, Padua, ITALY

3. Centro Interdipartimentale di Ricerca per lo Studio dei Materiali Cementizi e dei Leganti Idraulici (CIRCe), Università degli Studi di Padova, Padua, ITALY

4. Sezione di Tettonofisica e Sismologia, Istituto Nazionale di Geofisica e Vulcanologia, Rome, ITALY

*Corresponding author: Simone Masoch simone.masoch@gmail.com

Keywords

Fault zone rock; Cockade breccia; Fluidization; Inverse grading; Pressure growth; Alpine Corsica

Highlights

- Cockade breccias were found in transtensional brittle faults in Alpine Corsica.
- Core clasts show inverse grading within the slipping zones.
- Fluidization of granular fault rocks promotes elutriation of the finer clasts.
- Pressure growth controls formation of cockade breccias at shallow crustal levels.
- Cockade breccias are a geological marker of ancient seismic faulting.

Abstract

Few fault rocks are known to be associated undoubtedly with seismic faulting. Here, we investigated the formation mechanism of cockade breccias found in transtensional faults cutting marbles and quartzites from the Col de Teghime area (Alpine Corsica, France). Field surveys coupled

with detailed microanalytical investigations indicated that: (i) the core clasts of the cockades are composed of host rock fragments >310 μm in size that are suspended in the slipping zones and arranged in inverse grading; (ii) the concentric rims of the cockades show a cyclic zoning made of saddle dolomite + Mg-calcite + goethite + anatase; (iii) the cockade-bearing veins are associated with minor fault veins filled with fine fragments (< 300 μm in size) cemented by the same minerals of the cockade rims.

We propose that the cockade-bearing faults formed at shallow crustal depths (< 2 km) and recorded the main phases of the seismic cycle: (1) co-seismic fragmentation of the wall rocks in presence of fluids; (2) co-seismic fluidization of the rock fragments resulting in elutriation of the finer particles and formation of residual porous and well-sorted slipping zones, where cockades will nucleate. Inverse grading resulted from co-seismic shaking and shearing; (3) post-seismic to inter-seismic cementation by deposition of carbonate-rich rims due to slow mineral pressure growth, resulting in the suspension of the clasts within the slipping zones. The formation mechanism of cockade breccias proposed here provides an alternative view of earthquake-related processes in fluid-rich environments at shallow crustal depths.

1. Introduction

The study of fault zones exposed at the Earth's surface potentially allows geologists to investigate the deformation processes associated with the various phases of the seismic cycle, from co-seismic to inter-seismic (Cowan, 1999; Di Toro et al., 2012; Neimeijer et al., 2012; Rowe and Griffith, 2015; Scholz, 2019). Moreover, the microstructural, mineralogical and geochemical characterization and interpretation of fault rock assemblages may reveal important information about earthquake source processes and rupture dynamics, including estimates of the co-seismic fault strength or of the breakdown work, which in some cases cannot be retrieved through the inversion of seismic waves (Sibson, 1975; Chester et al., 2005; Di Toro et al., 2006). However, fault zone rocks are typically the result of long-lasting polyphase deformation and exhumation histories, which often result in the formation of fault rock assemblages that are difficult to associate with particular phases of the seismic cycles or with seismic vs. aseismic slip (Snoke et al., 1998; Cowan, 1999; Rowe and Griffith, 2015). A further complication rises from the presence of fluids, which alter fault rock assemblages but also play a pivotal role in fault and earthquake mechanics (Scholz, 2019). In practice, it is extremely difficult to estimate the pore fluid pressure and the permeability of fault zones at depth and during the several phases of the seismic cycle through the investigation of exhumed fault rocks (Caine et al., 1996; Faulkner et al., 2010). This is because a wide range of physical and chemical processes can modify the permeability of fault zone rocks throughout the seismic cycle. Qualitatively, when seismic ruptures propagate breaching fluid reservoirs at depth, fault zones behave as conduits allowing fluid discharge and, possibly, deposition of mineral ore bodies at geometrical fault zone complexities (e.g., breccias in dilational jogs: Sibson, 1985; 1986). On the other hand, episodic to cyclic ingressions of pressurized fluids (i.e., fault-valve behavior; Sibson, 1990) can trigger earthquakes and can be associated with swarm activity in mesh-like arrays of small faults and veins (i.e., high fluid-flux fault/fracture networks, Sibson, 1990; Dempsey et al., 2014; Cox and Munroe, 2016). Lastly, post- and inter-seismic precipitation of hydrothermal minerals in pores and fractures will progressively reduce the permeability and eventually seal the fault zone (Tenthorey et al., 2003; Cox, 2005).

A relatively common fault product in shallow crustal hydrothermal settings are cockade breccias, or low-temperature hydrothermal fault vein infills characterized by up to decimeter-sized clasts wrapped by concentric bands of cement (Frenzel and Woodcock, 2014 and references therein). Frenzel and Woodcook (2014) proposed six formation mechanisms for cockade breccias. Only two mechanisms are strictly associated with brittle faulting in presence of fluids: (i) repeated cockade accretion-rotation associated with fracturing and, (ii) sustained suspension of clasts in rapidly ascending fluids and simultaneous cement precipitation. The first mechanism provides evidence for syn-tectonic mineralization (Genna et al., 1996; Frenzel and Woodcock, 2014), while, the second implies the circulation of pressurized fluids associated with injection-driven swarm seismicity in high-flux dilatant faults (Cox and Munroe, 2016). Additional evidence supporting a relationship between cockade breccia formation and seismic faulting is the inverse grading of the core clasts of the cockades in some breccia layers, suggesting either self-organization of the core clasts controlled by seismic shaking (Genna et al., 1996) or variation of flow velocities during co-seismic fluidization of the fragmented rocks (Cox and Munroe, 2016). Even though cockade breccias have often been reported both in the ore and structural geology literature (Bastin, 1950; Kutina and Sedlackova, 1961; Genna et al., 1996; Leroy et al., 2000; Frenzel and Woodcock, 2014), to our knowledge there are few studies that attempt to relate their peculiar microstructures to particular phases of the seismic cycle (e.g., Cox and Monroe, 2016; Berger and Herwegh, 2019).

In this study, we describe cockade-bearing transtensional faults cropping out in Alpine Corsica (Col de Teghime, France). The fault core rocks include cockade breccias, often with inverse grading of the core clasts, cemented by hydrothermal minerals. Field structural geology surveys and detailed microstructural and mineralogical observations allowed us to associate the formation and development of cockade breccias with the main phases (i.e., co-seismic to inter-seismic) of the earthquake cycle.

2. Geological Setting

2.1 Alpine Corsica

Alpine Corsica is a Tethyan-type accretionary wedge composed of continent- and oceanic-derived units stacked together during the Alpine orogenesis (Vitale Brovarone et al., 2013 and references therein). Alpine Corsica is divided into three main structural domains (continental-derived units, Schistes Lustrés and Nappes Supérieures) sealed by Miocene sedimentary deposits (Durand-Delga, 1984). In particular, the Schistes Lustrés complex is mainly oceanic-derived and consists of metaophiolitic sequences from the Ligurian-Tethyan Ocean (mantle ultramafic rocks, metagabbros, pillow lava and associated metasedimentary cover of marbles, quartzites, calcschists, etc.) wrapping thin interlayered slices of continental basement rocks (granitoids and gabbro intrusions; Faure and Malavieille, 1981; Durand-Delga, 1984; Dallan and Puccinelli, 1995; Meresse et al., 2012).

Since the Late Cretaceous, east-dipping intra-oceanic subduction driven by the convergence of the Euro-Asia and Adria plates (i.e., Euro-Asia beneath Adria) formed an accretionary wedge by piling up slices of oceanic rocks and sedimentary cover (Molli, 2008 and references therein). In Alpine Corsica, this compressional stage was recorded by High Pressure – Low Temperature (HP-LT) metamorphism (Jolivet et al., 1990; Molli, 2008). Because of the Mid-Eocene slab break-off and the initiation of the Adria plate subduction, the active Apenninic margin began to roll back while migrating to the East, shifting the tectonic regime in Alpine Corsica from compressional to extensional (Molli and Malavieille, 2011).

Since the Oligocene, Alpine Corsica underwent multiple extensional stages due to the lithospheric extension controlled by the continued eastward migration of Apenninic subduction (Jolivet et al., 1990; Molli and Malavieille, 2011). The last extensional stage was recorded by Tortonian to Serravallian in age NW-SE and N-S trending high-angle brittle normal faults that accommodated at least 6 km of vertical throw in the Saint Florent area (Fellin et al., 2005; Cavazza et al., 2007, Gueydan et al., 2017).

2.2 Geology of the Col de Teghime area

In the Col de Teghime area, metasediments overlaying the continental granitoids of Serra di Pigno, a unit belonging to the Schistes Lustrés complex, crop out (Dallan and Puccinelli, 1995; Meresse et al., 2012). The metasediments are composed of quartzites, metabasites, micaschists, pure and impure marbles (Fig. 1a; see Meresse et al., 2012 for details). The contact between the metasediments and the granitoid basement is marked by mylonites with HP-LT paragenesis (Dallan and Puccinelli, 1995). Miocene NW-SE trending sub-vertical brittle fault zones crosscut the metasediments and the continental granitoids with transtensive or strike-slip kinematics (Fig. 1b). The cockade-bearing faults presented here are associated with this fault system.

3. Methods

Four fault zones exposed in the Col de Teghime area where studied in detail. Original field surveys along with published geological maps (Faure and Malavieille, 1981; Dallan and Puccinelli, 1995) were used to trace major lineaments in the area using ArcGIS 10.6 software. At the four selected localities, the attitudes and lineations of faults, veins, fractures and host rock foliations were systematically measured. Measurements of attitudes and lineations of faults, veins, fractures and host rock foliations were plotted onto stereonets (equal area, lower hemisphere) using Stereonet 10 (Allmendinger et al., 2011; Cardozo and Allmendinger, 2013). To describe fault zone rocks, we referred to the classifications proposed by Sibson (1977) and Woodcock and Mort (2008).

Twenty-six oriented fault rock samples were collected, and microstructural observations were conducted on thin sections cut perpendicular to the slip surfaces and fault vein boundaries and oriented either parallel or perpendicular to fault lineations. Transmitted-light optical microscopy (OM) was used to determine microstructural features at thin section scale, and to identify areas suitable for further microanalytical investigations. Scanning electron microscopy (SEM) was used to acquire high-resolution backscattered electron (BSE) images of the cockade breccias and coupled with semiquantitative energy dispersion spectroscopy (EDX) elemental analyses. Electron microscopy investigations were performed with SEM using a CamScan MX3000 operating at 25 kV at Department of Geosciences at Università degli Studi di Padova, and FE-SEM using either a FEI Quanta 650 operating at 15 kV at the University of Manchester, or FEI Quanta 200F operating at 20 kV at the Scientific Center for Optical and Electron Microscopy at ETH Zurich. Optical microscopy cathodoluminescence (OM-CL) was applied to obtain information on chemical variations within the cockade rims. The OM-CL was employed using a Nikon microscope equipped with a Nikon camera, installed at the Department of Geosciences in Padova, working at 15-17 kV and 200-230 μA in a vacuum of 0.18-0.20 Torr.

High-resolution mineral phase identification was performed using Micro-Raman spectroscopy, while the bulk mineralogy of the cockade breccias and veins was retrieved through X-ray powder diffraction (XRPD). Micro-Raman spectroscopy was performed with a 532-nm green laser (power of 3.0 mW) on polished thin sections using a Thermo Scientific DXR MicroRaman at the Department of Chemical Sciences (Padova). The obtained spectra (range of 100-3574 cm^{-1}) were elaborated with OMNIC Spectra software for baseline correction, eliminating the natural fluorescence of carbonate crystals and mineral phase identification. X-ray powder diffraction (XRPD) analyses were performed with a PANalytical X'Pert Pro diffractometer equipped with a Co radiation source, operating at 40 mA and 40 kV (Department of Geosciences, Padova) in the angular range $3° < 2\Theta < 85°$.

Micro X-ray Computed Tomography (micro-CT) was performed on three cylindrical samples (diameter × height = 5 × 5 mm) of the breccia to reconstruct the three-dimensional arrangement of the cockades using a Skyscan1172 tomograph installed at the Department of Geosciences (Padova). The device was equipped with an X-ray source with voltage range of 20-100 kV, power range of 8-10 W and a 11 Mp CCD detector. The scans of the samples were performed with a source voltage and current of 70 kV and 141 µA, respectively, a sample-to-source distance of 53.010 mm, and a camera-to-source distance of 211.545 mm; a 0.5 mm-thick Al filter was also applied. This resulted in sample images with a pixel size (spatial resolution) of 4.35 µm. A total number of 1442 radiographs per scan were acquired over a 360° rotation (angular step 0.3°, exposure 1050 ms). The reconstruction of cross-sectional slices from 2-D X-ray projections was carried out using a modified FDK algorithm (Feldkamp et al., 1984) for cone-beam geometry implemented in the Skyscan NRecon software. Corrections for the beam hardening effect and ring artefacts were also applied during the reconstruction process in order to improve image quality (Sijbers and Postnov, 2004; Boin and Haibel, 2006).

Image analysis was performed on high-resolution scans of thin sections (samples CC01-12 and CC11-17), BSE images (CC11-17) and micro-CT slices (CC01-12) using the software Fiji

(Schindelin et al., 2012) to determine the clast size distributions (CSDs) in two dimensions of the core clasts in the cockade-bearing faults. Since some core clasts and the sealing cement have similar mineralogy (dolomite), automatic segmentation of the clasts in BSE images and micro-CT slices was problematic; thus, all the clast boundaries were traced manually. The clasts size was defined as the diameter d of the circle with the equivalent area A of the clasts and expressed as $d=2(A/\pi)^{0.5}$. Due to the spatial resolution of the images used for the analysis, a cut-off value of 25 square pixels was defined. This corresponds to $d\sim30$ µm for the high-resolution scans of thin sections and $d\sim10$ µm for the BSE images and slices of the micro-CT analysis, because smaller clasts were not recognizable in the processed images. Resulting CSDs were obtained using the procedure described by Monzawa and Otsuki (2003) to define the cumulative number of clasts, N, larger than a given diameter. The CSD curve was plotted in a $log(N)$-$log(d)$ diagram and the distribution was described by the power-law relationship, $N \sim d^{-D}$ ($log(N) \sim -Dlog(d)$), where D represents the slope of the curve (Turcotte, 1986). Note that the investigated clast size range was too small (less than three orders of magnitude) to determine if the distribution was statistically self-similar. Instead, in this study, we determined D (i) to quantify the different CSDs of the clast fragments found in the cockade-bearing veins and, (ii) to compare these CSDs with those of the fine clasts-supported fault veins to discuss the formation mechanisms of the cockade breccias.

4. Cockade-bearing faults

4.1 Field observations

We focused here on two transtensional fault zones which are the best exposed in the study area. One fault zone is located on the eastern flank of Monte Secco (stop 1; 512 ± 3 m a.s.l.; 42°4’20.6” N, 9°22’51.7” E, Fig. 1). The outcrop extends for about 40 m in an abandoned quarry and offers a continuous exposure in a direction orthogonal to the strike of the fault zone. The main fault surface strikes from WSW-ENE to WNW-ESE with a mean value of N105° and dips 38° towards

NNE. Many fault slip surfaces, including the main one, have well-developed calcite slickenlines with dextral transtensive kinematics (mean pitch of 45° to the East, Fig. 1b). The main fault surface is lined by a reddish breccia fault core, up to 1 m thick, marking the contact between impure quartzites in the footwall block and silica-enriched marbles in the hanging wall block (Fig. 2). The damage zone is asymmetric: it is wider (up to 15 m thick) and more intensely deformed within the footwall quartzites compared to marble (up to 5 m thick) in the hanging wall. Brittle deformation within the damage zone is accommodated by joints and shear fractures, often filled by dolomite and calcite veins (Fig. 2a). In the hanging wall, minor brittle faults with normal dip-slip kinematics and the same mineral filling of the main fault (dolomite, calcite and goethite from XRPD analysis) accommodated up to 25-40 cm of normal dip-slip displacement (Fig. 2f) Locally, the fault core rocks are injected into the damage zone with veins up to tens of centimeters long (Fig. 2d). The fault core is composed mainly by breccias (rarely proto-breccias, following the classification proposed by Woodcock and Mort, 2008) cemented by a reddish- to brown-color fine matrix made of calcite and goethite (from XRPD analysis) and includes fragments of the wall rocks with dimensions up to ~10 cm (Fig. 2b). The breccia clasts are surrounded by cement rims forming a cockade-like texture. In this study, we distinguish cockade-bearing veins from cockade-bearing faults. The latter includes one or more cockade-bearing veins, cataclasites, principal slip surfaces, etc. In particular, the fault core and the cockade breccias have the following features:

- the cockade-bearing veins are ~3-4 cm thick (Fig. 2c);
- the core clasts of the cockades have inverse grading with the smallest clasts at the bottom and the largest ones at the top of the vein: see Fig. 2c-d);
- the core clasts of the cockades are very well-sorted with the largest and smallest clasts of ~1 cm and ~310 μm in size, respectively (see CSDs in section 4.3.3);
- sub-vertical veins departing from the slipping zones inject the footwall block and are filled with angular to sub-angular host rock fragments (Fig. 2d);

- the core clasts seem to be suspended within the reddish- to brown-color matrix (i.e., they are not in contact; Fig. 2c-d);
- locally, toward the top wall of the thicker cockade-bearing veins, the sealing is made of calcite instead of reddish in color matrix (Fig. 2c).

The other selected fault zone crops out on the western flank of the Monte Secco and Monte Rossi ridge (stop 2; 465 ± 3 m a.s.l.; 42°40’27.7” N, 9°22’20.7” E, Fig. 1). The fault zone is NW-SE trending, subvertical and exposed for 100-150 meters in an abandoned marble quarry where it cuts impure grey-colored marbles (Fig. 3a). The main fault surface is marked by well-developed calcite slickenlines and, locally, is a mirror-like surface sharply truncating clasts of the underlying breccias (Fig. 3). The fault core has an average thickness of 20 cm and is made of fault breccias well-cemented by a reddish matrix composed of calcite and goethite (XRPD analyses). The breccias have cockade-like texture with core clasts of ~5-10 mm in size wrapped by calcite- and dolomite-built rims (Fig. 3c-d). The cockade breccias of this fault zone do not show inverse grading.

4.2 Deformation history recorded in cockade-bearing faults

From the outcrop to the microscopic scale, the cockade-bearing faults recorded a complex deformation history. The cockade-bearing faults of the Col de Teghime area are not meant to necessarily record the same series of deformation events from one site to another and can potentially illustrate local complexities. For example, below we outline the series of veining and faulting events (V1 to V8 from older to younger, see Fig. 4a-b) recorded within a cockade breccia from stop 1 (Figs. 1a, 2), where these fault rocks are better exposed:

- V1: dense network of minor fractures and veins filled with brownish in color calcite, cutting the wall rocks;
- V2: minor faults marked by 50 μm-thick ultracataclastic slipping zones parallel to cockade-bearing veins (V3);
- V3: ~3-4 cm-thick cockade-bearing veins;

- V4: brown in color ultracataclastic fault veins filled by fine quartzite clasts that locally inject spatially related cockade-bearing veins (V3; Fig. 4a);
- V5-V6: multiple carbonate-bearing microveins cutting the host rocks and older veins and faults (V1-V4);
- V7: dolomite-bearing veins;
- V8: late precipitation of calcite cement, which partially sealed the cavities in the cockade breccias and in the fault core (Figs. 2e, 4, 5a-b).

A detailed microstructural and mineralogical investigation of selected samples was performed to characterize the cockade-bearing faults and further constrain the crosscutting relationships among the several veining and faulting events.

4.3 Microstructures and mineralogy of cockade-bearing faults

4.3.1. Optical and scanning electron microscope observations

Cockade-bearing veins contain core clasts of (i) host rock lithology and (ii) reworked fragments of older carbonate veins (V1; Figs. 4-7). At stop 1, the quartzite-built clasts are the most abundant (>95% in the studied samples), have an angular to sub-angular shape (partly rounded) and usually consist of cataclasite to ultracataclasite made of highly comminuted quartz grains with diameters of 60-10 μm (Figs. 4, 5a, 5e, 6a-b). Reworked-vein clasts are much less abundant (<5% in the studied samples) and consist of rhombohedral calcite and dolomite crystals of older vein cement containing few fine-grained quartzite fragments. The reworked-vein clasts tend to have elongated shapes (aspect ratio >2) but are randomly oriented with respect to the margins of the slipping zones (Figs. 4a, 6a-b). Both quartzite and reworked-vein clasts are well-sorted and disposed in inverse grading (see section 4.1). At stop 2, core clasts consist entirely of marble-built fragments (often of cataclasite) and do not show any grading distribution within the slipping zones (Fig. 7a-c). Cockade-bearing veins cut slipping zones filled with cortex-clast aggregates (CCAs; Figs. 7a, 7d-e) similar to those produced in rotary-shear experiments reproducing fault slip in calcite-built gouge (Rempe et al., 2014).

The clasts are surrounded by four concentric rims composed mainly of euhedral carbonate minerals (Fig. 5). From the core clast outwards, the rim-forming carbonate minerals are: (1) saddle dolomite, (2) Mg-calcite, (3) saddle dolomite and (4) Mg-calcite. With rare exceptions, each rim entirely wraps the core clast and the more internal rims. In detail:

- Rim 1 is 50 to 200 μm thick and made of euhedral saddle dolomite with homogeneous composition and extremely enriched in calcium and iron (semiquantitative EDX spot analysis). Close to the external border, intracrystalline pores <5 μm thick and parallel to the dolomite cleavage are common;
- Rim 2 is 50-150 μm thick and made of brown in color euhedral Mg-calcite. The brown color is due to the presence of goethite and anatase partially filling cleavage-parallel pores (Fig. 5c). Goethite and anatase appear as either spherulitic- or acicular-shaped crystals in the SEM-BSE images (Fig. 5f);
- Rim 3 is ~ 40 μm thick and made of zoned euhedral saddle dolomite enriched in calcium and iron. The rim does not have any goethite nor anatase crystals and has the ~10 μm-thick edges enriched in magnesium (dark gray in SEM-BSE images, Fig. 5a). Pores mimicking dolomite cleavage are common.
- Rim 4 is made of euhedral Mg-calcite and is rich in spherulitic and acicular crystals of goethite and anatase (Fig. 5a-b).

The cockades (core + rims) are separated by a late cement made of zoned, calcian saddle dolomite (Fig. 8a). Pores ranging from <100 μm to ~ 0.5 mm, locally filled by pure calcite with blocky-equant grains (V8; Fig. 5a), are present within the late sealing cement.

Brown in color ultracataclastic (clast size < 300 μm) fault veins (V4) are frequently associated with cockade-bearing veins (Fig. 8b-c): the fault veins V4 lay parallel to previous ultracataclasite-filled slipping zones (V2) or cut the cockade-bearing veins (Fig. 4). The fault veins V4 are filled by angular quartzite clasts cemented by calcian dolomite. Pores are frequent (< 20 µm in size) and partially sealed by goethite and anatase (Fig. 8c).

4.3.2 Cathodoluminescence observations

Saddle dolomite-built rims 1 and 3 show generally homogeneous dull red luminescence with sporadic bright red areas (Fig. 5d-e). In contrast, the Mg-calcite-built rims 2 and 4 have pronounced concentric zonings with luminescence varying between bright orange (indicative of higher Fe and lower Mn content) to yellow (indicative of higher Mn and lower Fe) (Götze, 2012 and references therein). The sealing cement is slightly more luminescent than the dolomite rims. However, the CL signal is generally saturated because of the high iron content (semi-quantitative EDX analysis) in the calcian dolomite (Fig. 5d-e). Lastly, the late pure calcite filling residual cavities (V8) are either zoned (Fig. 8d) or have a uniform bright luminescence (Fig. 5d).

4.3.3 Clast size distributions of the cockade cores

In all the analyzed samples, the upper limit of the CSD was represented by the largest clast and was affected by undersampling due to the limited extension of the investigated area (ca. 2 × 3 cm^2). The lower cut-off of the CSD curves was artificial only in the case of cockade-absent ultracataclasites (V4, sample CC01-12; Fig. 9) whose distributions suffer from undersampling for particles < 40 µm in size. For V4, the linear portion (range 40-200 µm in size) of the CSD curves has a slope $D \sim 2$ (Fig. 9). The lower cut-off of the CSDs curves of the cockade-bearing veins (V3) was representative of the real distribution, since there were very few clasts < 310 µm in size (see Figs. 4, 6b and bottom right corner of Fig. 8b). The CSDs of V3 are composed by two segments: (i) a steep slope segment for clasts size ranges of 310-690 µm (D=1.734; sample CC01-12) and 460-1.25×10^3 µm (D=1.604; sample CC11-17) and, (ii) a shallow slope segment (D<1) for clasts size ranges of 100-310 µm (CC01-12) and 80-460 µm (CC11-17) (Fig. 9). This CSD analyses indicate that the cockade-bearing veins consist almost entirely of core clasts larger 300-400 μm with very few finer particles.

4.3.4 3-D microtomography reconstructions

In 2-D views of the breccia samples, the core clasts appear to not be in contact (outcrop exposures and thin sections of V3, Figs. 2c-d, 3c-d, 4a, 6, 7a-c, bottom right corner of Fig. 8b). This observation, which is critical for the interpretation of these fault rocks, was tested with 3-D microstructural imaging derived from micro-CT analyses. Three cylindrical cores were drilled along a transect perpendicular to the vein walls to characterize the inverse grading in 3-D (see Fig. 10). The 3-D renderings were obtained with the Volume Viewer plugin available in Fiji software (Schindelin et al., 2012). The 3-D imaging of the cockade breccias confirms that the core clasts do not touch each other, and each cockade is separated from the others by calcian dolomite-built cement (Fig. 10a). The cockade rims entirely wrap the core clasts, always have intact crystal terminations (i.e., idiomorphic shape) and, locally, interfere each other forming triple junctions at the contact between the facing rims of adjacent cockades (Figs. 6c, 7c). The cockade rims are truncated by younger faults and veins cutting the cockade-bearing veins (V4-V7; Fig. 10b).

5. Formation of cockade-bearing faults

5.1 Co-seismic fragmentation in presence of fluids

Brittle deformation induced by earthquake ruptures is dominated by wall rock fragmentation, shattering and pulverization due to dynamic stress loading and, in the presence of fluids, abrupt pore pressure changes (Sibson, 1986; Dor et al., 2006; Reches and Dewers, 2005). These processes mainly occur at propagating fault rupture tips and at geometrical complexities, such as extensional jogs, where dilation breccias are frequently generated (Fig. 11a). Dilation breccias have been hypothesized to result from wall rock implosion because of the sudden volumetric decompression when a fault rupture reaches an extensional jog (Sibson, 1985; 1986). Implosion breccias generally display a shattered to crackle fabric with minimal displacement between the angular fragments of the wall rock (Sibson, 1986; Tarasewicz et al., 2005; Woodcock and Mort, 2008; Fondriest et al., 2015; 2017). In the cockade-bearing faults studied here, the core clasts have angular to sub-angular shapes and are well-sorted (Figs. 4, 5, 6, 7a-c, 9, 10), suggesting that implosion of the wall rock or dynamic stress wave loading fragmentation alone cannot explain the formation of these fabrics. Therefore, frictional sliding associated with abrasive processes within the slipping zones occurred and have possibly produced grain size reduction and chipping of the angular-shaped fragments of the wall rocks (Sibson, 1986) (Figs. 5, 6, 7b-c).

Cockade-bearing faults are associated with veins filled with carbonates (Fig. 4), suggesting that faulting occurred in the presence of CO_2-rich fluids. Since mobilization of fragmented granular material (breccias and gouge) is a common mechanism associated with co-seismic fluid injection within slipping zones (e.g., Monzawa and Otsuki, 2003, Smith et al., 2008; Fondriest et al., 2012), grain mobilization could have also favored both mechanical attrition processes, microfracturing and spallation, but also chemical wearing resulting in the removal of asperities and partial rounding of the clasts (Snoke et al., 1998; Blenkinsop, 2000; Oliver and Bons, 2001).

However, based on field and microstructural observations, the formation of the veins, where cockade breccias are found, might also result from hybrid fracturing and shearing in presence of pressurized fluids. We dismiss that the formation of core clasts resulted from brecciation due to gravitation collapse in dilatant fractures, since we never found any feature suggesting this origin, such as kinked bedding bordering the breccia veins (in our case, the foliated marbles, see Figs. 2-3) or sediment and clay filling (e.g., Walker et al, 2011; Woodcock et al., 2014).

In summary, since cockade-bearing veins (i) are bordered by host rocks with cataclastic fabric (Fig. 7), (ii) cut and are cut by principal slip surfaces (Fig. 3), (iii) include partly rounded fragments of the host rocks (quartzites and ultracataclasites; Figs. 5-6) and (iv) are associated with injection-like veins filled with angular to sub-angular host rock fragments (Fig. 2b-d), we conclude that they possibly formed by cataclastic processes in presence of pressurized fluids. Moreover, injection-like veins have been previously related to seismic faulting, as a result of rupture propagation (e.g., Rowe et al., 2012).

5.2 Co-seismic grain sorting and inverse grading

The CSDs of the core clasts in the cockade-bearing faults suggest that a grain sorting mechanism removed preferentially the smaller clasts (< 300-400 μm in size in average; Fig. 9). Furthermore, field and microstructural observations highlight that cockade-bearing veins are spatially associated and sometimes cut by fault veins filled by finer clasts (V4) (Fig. 4). The clasts in the fault vein V4 are smaller (< 300 μm in diameter) than in the cockade-bearing veins (see CSDs in Fig. 9). Their systematic association suggests that cockade-bearing veins and fault veins V4 may be formed by the same genetic processes. Below, we present a conceptual model that relates clast sorting and inverse grading different phases of the seismic cycle.

During rupture propagation and seismic slip, large and abrupt pore pressure changes may occur leading to fluid migration along fault and fluidization of fault materials (Sibson, 1986; 1990; Rowe et al., 2012). In a granular flow driven by fluidization, fluids have enough energy to transport clasts. How far the clasts can be sustained and transported by the fluids is a function of several variables, including clasts size: finer clasts can be transported farther compared to the larger ones, which are left behind as the fluid flow loses energy (Williams, 1976; Di Felice, 1995). According to this model, well-sorted fault rocks are formed with the larger clasts concentrated where the flow rates are larger and the smaller clasts are transported towards the end of the ruptured fault. Evidence of sorting in fault rocks resulting from fluidization has been reported both in natural faults and experimental fault gouges indicating that grain sorting is often associated with seismic faulting (e.g., Boullier et al., 2009; Fondriest et al., 2012; Cox and Munroe, 2016; see Fig. 9). It is reasonable to infer that the clasts found at the core of cockades in cockade-bearing veins may represent the clasts close to the source point of fragmentation and the smaller clasts in ultracataclastic fault veins V4 reflect the distal part of a fluid flow driven by a single release of fluids.

According to Cox and Munroe (2016), fluid velocities required for fluidizing particles and elutriating them can be estimated using the Ergun equation (Ergun, 1952) and the equation for turbulent flow proposed by Gaskell (1992). The Ergun equation relates the drag exerted on an aggregate of particles of diameter *d* by a fluid with superficial flow velocity u_s:

$$\frac{\Delta p}{L} = \frac{150\mu(1-\epsilon)^2 u_s}{\Psi^2\epsilon^3 d^2} + \frac{1.75(1-\epsilon)\rho u_s^2}{\Psi\epsilon^3 d} \qquad \text{(Eq. 1)}$$

where Δp is the fluid pressure drop; L is the height of the fluidized layer; ψ is the particle sphericity; ε is the porosity; and μ and ρ are the fluid viscosity and density. When the force exerted on particles by the upward flow of fluid equals the gravity force on the particles, the ratio between the fluid pressure drop and the height of the fluidized layer is given by:

$$\frac{\Delta p}{L} = (\rho_p - \rho)(1-\epsilon)g \qquad \text{(Eq. 2)}$$

where ρ_p is the particle density and g is the gravity acceleration (Di Felice, 1995). Therefore, Eqs. (1) and (2) can be combined and solved to estimate the minimum fluidization velocity u_m:

$$u_m = \frac{150\mu(\epsilon-1) + \sqrt{(150\mu(1-\epsilon))^2 + 7g\rho(\rho_p-\rho)\epsilon^3 d^3}}{3.5\rho d}. \qquad \text{(Eq. 3)}$$

For packed aggregates the porosity at minimum fluidization velocity (ϵ_{mf}) is empirically related to the particle sphericity as $\epsilon_{mf} = (0.071/\Psi)^{1/3}$ (Wen and Yu, 1966). The velocity required to elutriate spherical particles u_t is given by (Gaskell, 1992):

$$u_t = \sqrt{\frac{3(\rho_p - \rho)gd}{\rho}} \quad \text{(Eq. 4).}$$

Fluidized cockade-bearing fault rocks formed at temperatures ≤150°C and confining pressures < 50 MPa (see sections 5.3 and 6). For modelling the fluidization behavior, we assumed a water density and viscosity of 943 kg/m^3 and 1.9×10^{-4} Pa·s, respectively (NIST Standard Reference Database Number 69) and particle density of 2650 kg/m^3 (Fig. 12a). The estimated velocity required to elutriate clasts ≤ 310 µm was 0.13 m/s for spherical particles. At this velocity, spherical particles with diameter ≤ 2.3 cm were kept in suspension, consistent with what we observed in cockade-bearing faults of the Col de Teghime area. Indeed, the largest diameter for a cockade core clast was ~1 cm. Similar slipping zones with the finer particles almost completely absent have been previously reported in the literature, for example, in the Borcola Fault Zone (Southern Alps, Italy) where Fondriest et al. (2012) proposed that fluidization and elutriation of particles < 300 µm result in the formation of peculiar grain sorting within the slipping zones (see Fig. 9 for CSDs comparison). This simplified fluidization model predicts sorting behavior that is consistent with our microstructural observations and we can explain the well-sorted CSDs with a combination of hydrodynamic processes leading to fluidization of granular fault rocks and elutriation of the finer fraction.

Some cockade-bearing faults present inverse grading of the core clasts (Figs. 2c-d, 4). Inverse grading within individual fault-rock units is reported in different tectonic settings (Boullier et al., 2009) as well as for cockade breccias (Genna et al., 1996; Cox and Munroe, 2016). A possible explanation for inverse grading in fault rocks is the Brazil-Nut Effect (also called “Muesli Effect”) controlled by repeated seismogenic shacking (Genna et al., 1996; Frenzel and Woodcock, 2014). The Brazil-Nut Effect has been deeply studied in material sciences with experimental and numerical modeling approaches (e.g., Rosato et al., 1987). Due to the collision of particles within a vibrating vessel, the concentration of larger particles in the upper side of the vessel is governed by kinematic sieving and, thus, the smaller particles settle down towards the bottom (Fig. 12b). Alternatively, Cox and Munroe (2016) proposed that inverse grading of the cockade breccias layers in the Rusey fault zone (North Cornwall, UK) and Roamane fault zone (Porgera, Papua New Guinea) was driven by variations in fluid velocity in fluidized breccias due to the slower flow along the walls of fluid conduits. Lastly, inverse grading may also result from simple shear of particles both in dry conditions and in presence of fluids (Williams, 1976; Siman-Tov and Brodsky, 2018): in a mixture of particles of different size, smaller particles pass through the void space more easily than the larger ones. Thus, shearing of particles promotes downward motion of the smaller ones leading to size segregation (Fig. 12c).

To summarize, it is not possible to exclude that Brazil-Nut Effect and simple shear operate together in the formation of inverse grading. Surely, in a fluidized-granular flow, collision between particles and shearing are possibly leading to a vertical organization with the larger particles towards the hanging wall. However, we prefer co-seismic fluidization of granular fault rocks and elutriation of finer clasts as the primary mechanism leading to the inverse grading and grain sorting in the studied cockade-bearing faults (Fig. 11a-b).

5.3 Post-seismic to inter-seismic pressure growth

The formation of cockade breccias requires the presence of pore space between core clasts to develop the cockade rims. Therefore, once cockades start to grow, the core clasts are separated (Genna et al., 1996; Frenzel and Woodcock, 2014; Cox and Munroe, 2016). Indeed, the 3-D micro-CT rendering reconstructions proved that clasts at the core of cockades are not in contact (Fig. 10) but are separated by concentric rims of saddle dolomite (rims 1 and 3) and Mg-calcite associated with microcrystals of goethite and anatase (rims 2 and 4; Fig. 5). Another necessary condition for formation of cockade breccias is ingression of fluids among the core clasts leading to precipitation of the cockade rims. As reviewed by Frenzel and Woodcock (2014), several physical and chemical processes lead to the formation of such a particular breccia. The authors pointed out that six mechanisms promote the formation of cockade-like texture: (i) cut effect (actually, this is not a mechanism of formation), (ii) partial metasomatic replacement of clast minerals, (iii) infall of clasts during cementation, (iv) pressure growth of minerals, (v) repeated cockade rotation-accretion associated with fracturing, and (vi) sustained suspension of clasts in rapidly ascending fluids and simultaneous cementation. Our 3-D micro-CT reconstructions dismiss that the core breccias studied here are related to cut effect ("mechanism" i) due to the 2-D nature of outcrop cuts and thin sections (Fig. 10). Based on our field, microstructural and mineralogical observations, we can exclude that fluid-rock interaction promoting concentric replacement of the pristine clast minerals occurred to form the cockade-bearing faults in the Col De Teghime area (mechanism ii). Infall of clasts during cementation (mechanism iii) should generate asymmetric rims, which is inconsistent with the symmetric concentric rims observed in our samples. Thus, one or more of the other mechanisms (iv to vi) or other unknown ones control the formation of cockade breccias from the Col de Teghime area.

Rim precipitation may start while the core clasts are kept in suspension in the fluid flow (i.e., fluidized flow behavior in Fig. 12a). Cox and Munroe (2016) described similar microstructures to those presented here, and proposed that growth of cockades rims occurred simultaneously to suspension of core clasts during fluidization of the granular fault rocks. This scenario implies that either (i) formation of carbonate-built rims occurred with fast, almost instantaneous, precipitation rates or (ii) the core clasts were kept in suspension for a long time span leading to the formation of such zoned carbonate-built rims. In the first case, experiments of hydrothermal flows showed that microcrystalline quartz can precipitate from supersaturate fluids in few minutes, when pressurized fluids were continuously pumped within a vessel partly filled with rock fragments where silica minerals precipitated (Okamoto et al., 2010). Recent flash depressurization experiments suggested that amorphous silica nanoparticles are produced instantaneously by explosive flash vaporization (Amagai et al., 2019). The amorphous nanoparticles crystallized into quartz grains of 1-2 μm and 10-20 μm in size after 1 and 15 days, respectively. Unfortunately, there are no experimental data regarding precipitation of carbonates from super-saturated solutions induced by rapid depressurization. Also modelling of the precipitation rates is poorly constrained because it is controlled by several poorly known parameters (e.g., temperature, pressure, pH, presence of impurities, level of saturation) in natural faults. Perhaps precipitation rates of carbonate minerals comparable to a co-seismic instantaneous precipitation are approached during fast travertine growth due to sudden degassing of water supersaturated in calcium carbonate. In this case, carbonate precipitation rate reaches values of ~0.3 μm/s (i.e., 10 m/yr; Chafetz and Folk, 1984). However, this particular precipitation rate is achieved when droplets of water supersaturated in calcium carbonate are suddenly vaporized because of an impact on a surface (i.e., waterfall environment): these are clearly different conditions from those occurring during seismic faulting. Based on these limited evidences, though we cannot exclude that the formation of the rims of the cockades occurred during seismic slip and associated fluid flow, this formation mechanism seems unlikely because of the too low precipitation rates. In the second case (hypothesis that the core clasts were kept in suspension for a long time span leading to the formation of such zoned carbonate-built rims), based on the modelling presented in section 5.2, the flow velocity to keep particles in suspension might have reached values around 10^{-1} m/s (Fig. 12a). The critical question is how long such high-flow velocities can be attained and sustained in a fault-related hydrothermal system. In fault-related hydrothermal systems, fluid flow is intermitted because of fault-valve processes linked to seismic activity (Sibson, 1981; 1990). Since such a high flow velocity can occur for short periods of time (i.e., during the peak of the fluid flow) due to the release of fluids during the seismic event, it is unrealistic that core clasts were continuously kept in suspension for the time span required to form thick and chemically zoned cockade rims. Alternatively, according to the model by Cox and Munroe (2016), injection-driven swarm sequences can produce the high fluid fluxes necessary to both keep in suspension continuously the core clasts and simultaneously form the cockade rims in all the directions. In this case, the core clasts are repeatedly fluidized and it should be expected that cockades rotate and interact with each other during suspension and settle down and start to be cemented when the fluid pressure is reduced. These processes would affect the symmetry of the concentric cockade rims and potentially lead to their breakage. We have never observed such microstructural evidence in the cockade breccias of the

Col de Teghime area. Moreover, the lack of symmetric distribution of core clasts within the slipping zones with the finer ones close to the vein boundaries and the larger ones in the central part of the vein due to the velocity gradient within the vein, as found by Cox and Munroe (2016) and the presence of triple junctions at the contact between adjacent cockades (see Figs. 6c, 7c) dismiss the possibility that the driving mechanism controlling the formation of cockade breccias presented here is the combination of simultaneous suspension of the core clasts and precipitation of the carbonate-built rims. Lastly, there is no evidence for long-lasting and large fluid circulation (= meter-thick vein deposits) associated with the NW-SE trending fault system in the area of the Col de Teghime.

Based on the points discussed above, we speculate that pressure growth (also called crystallization pressure; Weyl, 1959) is the main mechanism compatible with the formation of the microstructures in the cockade breccias of the Col de Teghime area (Fig. 11c). Indeed, mineralogical and chemical zonings can easily develop in longer time spans, suggesting that the formation of the cockade rims occurred during the post-seismic to inter-seismic phase of the seismic cycle (from months to thousands of years; Scholz, 2019), when the fault zone sealed due to the infiltration of chemically diverse fluids. Pressure growth develops crystal faces projecting in all the directions if the mineral phases have high surface energy and surface energy anisotropy (e.g., pyrite vs. quartz or calcite and quartz; Spry, 1969). Another observation consistent with pressure-growth mechanism is the lack of any deformation of the cockade rims. For instance, truncation of concentric rims has been proposed as indicator of cockade breccias resulting from rotation-accretion mechanism and suggesting syntectonic cockade breccia formation (Genna et al., 1996; Frenzel and Woodcock, 2014; Berger and Herwegh, 2019). Moreover, pressure growth of crystals in stationary condition within pressurized fluids is compatible with the hypothesis that core clasts were separated from each other without any remarkable modification of the clast arrangement (inverse grading) derived from the previous sorting of the fluidized granular material during seismic slip. Importantly, experimental evidence shows that pressure growth in rocks can uplift a dead weight (Taber, 1916; Gratier at al.,

2012) and achieve magnitudes of 30 MPa or larger (Zheng et al., 2018; 2019, in the case of reaction-induced fracturing) resulting in fracturing of porous rocks (Noiriel at al., 2010).

Microstructural observations indicate that, in each cockade, the rims surround completely the core clasts and each rim grows in epitaxial way over the previous one. This suggests that concentric carbonate-built rims are free to grow in a highly porous medium with low packing forming perfect euhedral facets in all the directions (Fig. 11c). Initial accretion of the rims, possibly initiated during seismic slip, derives from supersaturated fluids promoting dolomite precipitation, then the accretion with epitaxial growth is governed by lower levels of supersaturation inhibiting ongoing nucleation and promoting the growth of concentric rims in all the directions. Indeed, epitaxial growth in presence of fluids is the most energetically favorable process of crystal growth as proved by experiments and numerical modeling (Putnis and Putnis, 2007; Mithen and Sear, 2014). On the other side, in fault veins with abundant ultrafine clasts (V4; see Figs. 8b-c, 10b) which act as multiple seeds for crystal precipitation and where the pore space between clasts is reduced, the epitaxial growth of concentric carbonate rims and the formation of cockades are inhibited.

Frenzel and Woodcock (2014) argued that cockade breccias resulting from pressure growth of crystals can form only in open spaces in subaerial environments where well-developed crystals can growth facets projecting outwards from the core clasts. However, the network of faulting and veining events cutting the cockade-bearing faults cannot form at the Earth's surface (see Fig. 2c-d, 4, 7a). Moreover, in hydration reactions (e.g., $CaO+H_2O \rightarrow Ca(OH)_2$ or slow explosive cement) the pressure induced by crystal growth exceeds 20-30 MPa. These experimental observations are also supported by conceptual and thermodynamic models suggesting that local significant crystallization pressures (up to 10s MPa) can be associated with supersaturated fluids both in diagenetic environments and in high-fluid pressure crack-sealing veining (the latter case is consistent with our study; Maliva and Siever, 1988; Wiltschko and Morse, 2001). If similar pressure magnitudes are achieved during the growth of dolomite and calcite, then cockades growth may easily occur at 1-2 km depth.

Presence of saddle dolomite in the cockade cement suggests that carbonate precipitation occurred between 60°C and 150°C (Warren, 2000 and references therein). The origin of CO_2-rich fluids may be various (meteoric, hydrothermal, mantle, mixing etc.) and would require further analyses that are outside the scope of this paper to be constrained. The high content of Fe in the carbonate cement and widespread precipitation of goethite suggest that fluids were enriched in Fe. Instead, variations in mineral composition in the concentric rims and the sealing cement may reflect fluctuations in fluid saturation levels. Mineralogical investigations highlight that saddle dolomite is enriched in Ca and Fe. At rapid growth rates, dolomite shows strong enrichment of Ca and slight enrichment of Fe over Mg related to high temperature conditions promoting the formation of non-stoichiometric dolomite (Searl, 1989). Further evidence of relatively rapid crystallization rate is the widespread presence of cavities in the dolomite cement (Fig. 5) which indicates that the growth rate of cockade rims was slightly higher than the precipitation rate, but did not proceed at co-seismic instantaneous precipitation rates (e.g., Bons et al., 2012).

6. Implications for the mechanics of cockade-bearing faults

Based on field and microstructural observations, each cockade-bearing vein recorded a single slip event (Figs. 4, 7a). The cockade-bearing faults are cut by other slip surfaces and slipping zones, suggesting that the fault cores accommodated multiple slip events (Figs. 3c, 4, 7a). Though we could not determine the displacement accommodated by the studied cockade-bearing faults because of limitations in the outcrop exposures, we did constrain the vertical displacement accommodated by the cockade-bearing faults from meters to tens of meters based on the following field evidences:

(i) several NW-SE trending cockade-bearing faults separate the contact between the continental granitoids and the quartzites and calcschists by tens of meters (see Fig. 1);

(ii) minor brittle faults in the hanging wall and with the same kinematics and mineral filling of the main fault in Fig. 2 accommodated up to 25-40 cm of normal displacement, suggesting larger slips for the main cockade-bearing fault.

The NW-SE trending fault system, which the cockade-bearing faults belong to, cuts the HP-HT units of the Schistes Lustrés and was exhumed 14-10 Ma according to fission track data (Fellin et al., 2005; 2006). Additionally, in the fault zone at stop 2 (Figs. 1, 3), slipping zones with CCAs are cut by the cockade-bearing slipping zones (Fig. 7). CCAs in calcite gouges were experimentally produced only at low normal stress (< 5 MPa; Rempe et al., 2014) and found in natural faults in the Italian Central Apennines exhumed from < 2 km depth (Smith et al., 2011). Consequently, the presence of cockade-bearing veins cutting the CCAs-bearing slipping zones suggests that the cockade-bearing faults were exhumed from shallow crustal levels. In conclusion, since the studied faults zones are late Miocene in age, this limits the depth of the cockade-bearing faults to less than 2 km.

At shallow crustal levels (< 2 km), low mean stresses and the necessary porosity (i.e., open space between the core clasts) allow pressure growth to operate and build the cockades. Otherwise, at deeper levels, compaction of the core clasts and mineral growth competition might impede the formation of such symmetric cockade rims by pressure growth. However, the formation of such idiomorphic cockade rims controlled by pressure growth imply nearly hydrostatic loading conditions, otherwise significant deviatoric stresses would control rims formation with mineral growth parallel to direction of minimum compressive stress (i.e., σ_3; see Cox and Munroe, 2016). This suggests that the cockade-bearing faults of the Col de Teghime were maintained relatively pumped by fluids at shallow crustal level (< 2 km, low mean stresses). Moreover, the cockade breccias of the Col de Teghime area mainly formed at fault geometrical irregularities (i.e., fault dilatant sites; e.g., Holland et al., 2006; 2011; von Hagke et al., 2019; see Fig. 2), which were relatively unloaded compared to the rest of the fault. In an extreme case, the core clasts produced and suspended by fluids at fault dilatant sites during the seismic event were left in a pool-like cavity close enough to the surface to allow them to remain open (i.e., the shoulders of the cavity sustained the load). This environment is similar to the one typical of pisoids formation, large (>2 mm) carbonate grains formed by accretion of carbonate wrapping pre-existing nuclei (Melim and Spilde, 2018 and references therein) in cave environments. Kettermann et al. (2019) proposed that tectonic caves can be produced till 800 m depth in deep dilatant zones, where host rock fragments and sediments collapse filling partially or entirely the cave system. At this depth, open fissures and tabular tilted blocks (see Kettermann et al., 2019 for their definition) can evolve in faults because of transition of failure modes from the tensile mode to the shear mode (Holland et al., 2006; 2011; von Hagke et al., 2019). In fact, though we dismiss that the formation of core clasts in the cockade breccias resulted from gravitation collapse in dilatant fractures, we cannot exclude that some of the faults discussed here become open fractures in their very shallow sections.

No reworked cockades were found as core clasts within the slipping zones of the Col de Teghime area. Instead, cockade-bearing faults are cut through by other fault veins (V4). This suggests that post-seismic cement precipitation promoted hardening of the slipping zones, lowering permeability and porosity of the granular fault rocks and increasing their strength and cohesion close to the values of the intact host rocks. This was previously proposed for fault zones in crystalline protoliths such as the Gole Larghe Fault Zone (Italian Southern Alps; Di Toro and Pennacchioni, 2005). Thus, at shallow crustal levels (i.e., at relative low confining stress), hydrothermal precipitation and formation of cockade breccias may represent a fault hardening process inhibiting seismic reactivation of preexisting slipping zones and promoting the nucleation and propagation of seismic faulting on newly formed slipping zones. Such a process has significant implications for the evolution of the fault zone architecture and the long-term mechanical behavior of fault zone.

7. Conclusions

We described cockade-bearing transtensional faults in Col de Teghime area (Alpine Corsica). The combination of field structural surveys and detailed microstructural and mineralogical observations allowed us to build a conceptual model for the formation of cockade breccias. The model includes the main phases of the seismic cycle:

1. Co-seismic fragmentation of the wall rocks at geometrical irregularities (e.g., dilation jogs) in the presence of CO_2- and Fe-rich fluids and mechanical wear leading to the formation of core clasts.
2. Co-seismic fluidization of the rock fragments resulting in grain elutriation and sorting of the finer clasts (found in fault veins V4 possibly associated with the distal parts of the fluidized clasts), and promoting the development of inverse grading within the slipping zones. Inverse grading of well-sorted and larger grains is possibly due to either collision between clasts (Brazil-Nut Effect) and shearing.
3. Formation and separation of cockades during the post-seismic to inter-seismic phase driven by pressure growth which controls the precipitation of concentric rims made from the interior to the exterior of (1) saddle dolomite, (2) Mg-calcite, (3) saddle dolomite and (4) Mg-calcite. In rims 2 and 4, goethite and anatase crystals are found in micropores mimicking the habit of the carbonate minerals. Saddle dolomite enriched in Ca and the widespread presence of pores in the dolomite cement suggests that cockade-bearing faults experienced relatively rapid crystallization rate.

The development of cockades is strongly controlled by the availability of free pore space between particles and grain size. Indeed, ultrafine and highly packed clasts inhibit the development of cockade breccias, as it was found in fault veins V4 which were interpreted as the distal part of elutriated clasts from co-seismic fluidization. In the cockade-bearing faults, the presence of open cavities and filling by calcite may support the hypothesis of late infiltration of meteoric fluids.

According to this study, and differently from previously published ones, pressure growth can control the formation of cockade breccias also at shallow depths (< 2 km) in the Earth’s crust. Moreover, according to our observations and those reported in previous studies, hydrodynamic elutriation seems to be a common mechanism for the formation of well-sorted fault rocks (i.e., breccias and cataclasites) lacking sub-millimeter-sized particles. Finally, cockade breccias may allow us to investigate the mechanical and chemical processes operating during the seismic cycle at shallow crustal levels in fluid-rich tectonic settings.

Acknowledgements

We thank Leonardo Tauro and Elena Masiero (thin section preparation), Federico Zorzi (XRPD analysis), Stefano Castelli and Nicola Michelon (high-resolution scans of thin sections), Lorenzo Raccagni (polished samples), and Luiz Grafulha Morales (technical support using FE-SEM at ScopeM). The authors thank Bob Holdsworth and an anonymous reviewer for their constructive criticism that improved the original manuscript. Of course, we remain responsible for the views reported in this study. The authors thank Brandon Vanderbeek for his friendly review of the manuscript. The authors thank also Tom Mitchell, Elena Spagnuolo, Giulio Viola, Cristiano Collettini, Matthew Tarling and Rodrigo Gomila for their helpful discussions. SM, MF and GDT acknowledge the ERC CoG 614705 NOFEAR project.

References

Allmendinger, R.W., Cardozo, N.C., Fisher, D., 2011. Structural Geology Algorithms: Vectors & Tensors. Cambridge University Press, Cambridge, England.

Amagai, T., Okamoto, A., Niibe, T., Hirano, N., Motomiya, K., Tsuchiya, N., 2019. Silica nanoparticles produced by explosive flash vaporization during earthquakes. Scientific Reports 9:9738. doi: https://doi.org/10.1038/s41598-019-46320-7.

Bastin, E.S., 1950. Interpretation of Ore Textures. Geological Society of America, Washington, DC.

Berger, A., Herwegh, M., 2019. Cockade structures as a paleo-earthquake proxy in upper crustal hydrothermal systems. Scientific Reports 9:9209. doi: https://doi.org/10.1038/s41598-019-45488-2.

Blenkinsop, T., 2000. Deformation microstructures and mechanisms in minerals and rocks. Kluwer Academic Publishers, Dordrecht, The Netherlands, 150 pp.

Boin, M., Haibel, A., 2006. Compensation of ring artefacts in synchrotron tomographic images. Optics Express, 14 (25) 12071-12075.

Bons, P.D., Elburg, M.A., Gomez-Rivas, E., 2012. A review of the formation of tectonic veins and their microstructures. Journal of Structural Geology 43, 33–62. doi:https://doi.org/10.1016/j.jsg.2012.07.005.

Boullier, A.M., Yeh, E.C., Boutareaud, S., Song, S.R., Tsai, C.H., 2009. Microscale anatomy of the 1999 Chi-Chi earthquake fault zone. Geochemistry, Geophysics, Geosystems 10. doi:10.1029/2008GC002252.

Caine, J.S., Evans, J.P., Forster, C.B., 1996. Fault zone architecture and permeability structure. Geology 24, 1025–1028. doi:10.1130/0091-7613(1996)024<1025:FZAAPS>2.3.CO;2.

Cavazza, W., DeCelles, P.G., Fellin, M.G., Paganelli, L., 2007. The Miocene Saint-Florent Basin in northern Corsica: stratigraphy, sedimentology, and tectonic implications. Basin Research 19, 507–527. doi:https://doi.org/10.1111/j.1365-2117.2007.00334.x.

Cardozo, N., Allmendinger, R.W., 2013. Spherical projections with OSXStereonet. Computers & Geosciences 51, 193–205. doi:10.1016/j.cageo.2012.07.021.

Chafetz, H.S., Folk, R.L., 1984. Travertines; depositional morphology and the bacterially constructed constituents. Journal of Sedimentary Research 54, 289–316. doi: https://doi.org/10.1306/212F8404-2B24-11D7-8648000102C1865D

Chester, J. S., Chester, F. M., Kronenberg, A. K., 2005. Fracture surface energy of the Punchbowl Fault, San Andreas system. Nature, 437, 133-135. doi:10.1038/nature03942.

Cowan, D.S., 1999. Do faults preserve a record of seismic slip? A field geologist’s opinion. Journal of Structural Geology 21, 999–1001. doi:https://doi.org/10.1016/S0191-8141(99)00046-2.

Cox, S.F., 2005, Coupling between deformation, fluid pressures and fluid flow in ore-producing hydrothermal environments. *In* Hedenquist, J.W., Thompson, J.F.H., Goldfarb, R.J. and Richards, J. P., editors, Economic Geology, 100th Anniversary Volume, Littleton, Society of Economic Geologists, p. 39–75.

Cox, S.F., Munroe, S.M., 2016. Breccia formation by particle fluidization in fault zones: Implications for transitory, rupture-controlled fluid flow regimes in hydrothermal systems. American Journal of Science 316, 241–278. doi:https://doi.10.2475/03.2016.02.

Dallan, L., Puccinelli, A., 1995. Geologia della regione tra Bastia e Saint-Florent (Corsica settentrionale) (con carta geologica alla scala 1:25.000). Bollettino Della Società Geologica Italiana 114, 23–66.

Dempsey, E.D., Holdsworth, R.E., Imber, J., Bistacchi, A., Di Toro, G., 2014. A geological explanation for intraplate earthquake clustering complexity: The zeolite-bearing fault/fracture networks in the Adamello Massif (Southern Italian Alps). Journal of Structural Geology 66, 58-74. doi:https://doi.org/10.1016/j.jsg.2014.04.009.

Di Felice, R., 1995. Hydrodynamics of liquid fluidisation. Chemical Engineering Science 50, 1213–1245. doi:https://doi.org/10.1016/0009-2509(95)98838-6.

Di Toro, G., Hirose, T., Nielsen, S., Pennacchioni, G., Shimamoto, T., 2006. Natural and experimental evidence of melt lubrication of faults during earthquakes. Science 311, 647-649.

Di Toro, G., Mittempergher, S., Ferri, F., Mitchell, T.M., Pennacchioni, G., 2012. The contribution of structural geology, experimental rock deformation and numerical modelling to an improved understanding of the seismic cycle: Preface to the Special Volume “Physico-chemical processes in seismic faults”. Journal of Structural Geology 38, 3–10. doi:https://doi.org/10.1016/j.jsg.2012.01.025.

Di Toro, G., Pennacchioni, G., 2005. Fault plane processes and mesoscopic structure of a strong-type seismogenic fault in tonalites (Adamello batholith, Southern Alps). Tectonophysics 402, 55-80. doi:https://doi.org/10.1016/j.tecto.2004.12.036.

Dor, O., Ben-Zion, Y., Rockwell, T.K., Brune, J., 2006. Pulverized rocks in the Mojave section of the San Andreas fault zone. Earth Planetary Science Letters 245, 642–654.

Durand-Delga, M., 1984. Principaux traits de la Corse Alpine et correlations avec les Alpes Ligures. Memorie della Societa Geologica Italiana 28, 285–329.

Ergun, S., 1952. Fluid flow through packed columns. Chemical Engineering Progress 48, n. 2, 89–94.

Faulkner, D.R., Jackson, C.A.L., Lunn, R.J., Schlische, R.W., Shipton, Z.K., Wibberley, C.A.J., Withjack, M.O., 2010. A review of recent developments concerning the structure, mechanics and fluid flow properties of fault zones. Journal of Structural Geology 32, 1557–1575. doi:https://doi.org/10.1016/j.jsg.2010.06.009.

Faure, M., Malavieille, J., 1981. Etude structurale d’un cisallement ductile: le charriage ophiolitique Corse dans la région de Bastia. Bulletin de la Société Géologique de France 23, 335–343.

Feldkamp, L.A., Davis, L.C., Kress, J.W., 1984. Practical cone-beam algorithm. Journal of the Optical Society of America A 1, 612-619.

Fellin, M.G., Picotti, V., Zattin, M., 2005. Neogene to Quaternary rifting and inversion inCorsica: retreat and collision in the western Mediterranean. Tectonics 24.

Fellin, M.G., Vance, J., Garver, J., Zattin, M., 2006. The thermal evolution of Corsica as recorded by zircon fission-tracks. Tectonophysics 421, 299–317. doi:https://doi.org/10.1016/j.tecto.2006.05.001.

Fondriest, M., Aretusini, S., Di Toro, G., Smith, S.A.F., 2015. Fracturing and rock pulverization along an exhumed seismogenic fault zone in dolostones: the Foiana Fault Zone (Southern Alps Italy). Tectonophysics 654, 56–74.

Fondriest, M., Doan, M-L., Aben, F., Fusseis, F., Mitchell, T.M., Voorn, M., Secco, M., Di Toro, G., 2017. Static versus dynamic fracturing in shallow carbonate fault zones. Earth and Planetary Science Letters 461, 8-19. doi:https://doi.org/10.1016/j.epsl.2016.12.024.

Fondriest, M., Smith, S.A., Di Toro, G., Zampieri, D., Mittempergher, S., 2012. Fault zone structure and seismic slip localization in dolostones, an example from the Southern Alps, Italy. Journal of Structural Geology 45, 52–67. doi:https://doi.org/10.1016/j.jsg.2012.06.014.

Frenzel, M., Woodcock, N.H., 2014. Cockade breccia: Product of mineralisation along dilational faults. Journal of Structural Geology 68, 194–206. doi:https://doi.org/10.1016/j.jsg.2014.09.001.

Gaskell, D. R., 1992, An Introduction to Transport Phenomena in Materials Engineering: New York, Macmillan, 637 p.

Genna, A., Jébrak, M., Marcoux, E., Milési, J.P., 1996. Genesis of cockade breccias in the tectonic evolution of the Cirotan epithermal gold system, West Java. Canadian Journal of Earth Sciences 33, 93–102.

Gratier, J.P., Frery, E., Deschamps, P., Røyne, A., Renard, F., Dysthe, D., Ellouz-Zimmerman, N., Hamelin, B., 2012. How travertine veins grow from top to bottom and lift the rocks above them: The effect of crystallization force. Geology 40, 1015. doi:10.1130/G33286.1.

Götze, J., 2012. Application of Cathodoluminescence Microscopy and Spectroscopy in Geosciences. Microscopy and Microanalysis 18, 1270–1284.

Gueydan, F., Brun, J.P., Phillippon, M., Noury, M., 2017. Sequential extension as a record of Corsica rotation during Apennines slab roll-back. Tectonophysics 710-711, 149–161. doi:https://doi.org/10.1016/j.tecto.2016.12.028.

Holland, M., Urai, J.L., Martel, S., 2006. The internal structure of fault zones in basaltic sequences. Earth Planetary Science Letters 248, 301–315.

Holland, M., Van Gent, H.W., Bazalgette, L., Yassir, N., Hoogerduijn-Strating, E. H., Urai, J.L., 2011. Evolution of dilatant fracture networks in normal faults – evidence from 4D model experiments. Earth Planetary Science Letters 304, 399–406. doi: 10.1016/j.epsl.2011.02.017.

Jolivet, L., Duboisl, R., Fournier, M., Goffe, B., Michard, A., Jourdan, C., 1990. Ductile extension in Alpine Corsica. Geology 18, 1007–1010. doi:https://doi.org/10.1130/0091-7613(1990)018<1007:DEIAC>2.3.CO;2.

Kettermann, M., Weismüller, C., von Hagke, C., Reicherter, K., Urai, J.L., 2019. Large near-surface block rotations at normal faults of the Iceland rift: Evolution of tectonic caves and dilatancy. Geology 47 (8), 781–785. doi:https://doi.org/10.1130/G46158.1.

Kutina, J., Sedlackova, J., 1961. The role of replacement in the origin of some cockade textures. Economic Geology 56, 149e176.

Lemmon, E.W., McLinden, M.O., Friend, D.G.. "Thermophysical Properties of Fluid Systems" in NIST Chemistry WebBook, NIST Standard Reference Database Number 69, Eds. P.J. Linstrom and W.G. Mallard, National Institute of Standards and Technology, Gaithersburg MD, 20899, https://doi.org/10.18434/T4D303, (retrieved October 26, 2018).

Leroy, J.L., Hube, D., Marcoux, E., 2000. Episodic deposition of Mn-minerals in cockade breccia structures in three low-sulfidation epithermal deposits: a mineral stratigraphy and fluid inclusion approach. Canadian Mineralogist 38, 1125-1136.

Maliva, R.G., Siever, R., 1988. Diagenetic replacement controlled by force of crystallization, Geology 16, 688–691.

Melim, L.E., Spilde, M.N.,2018. A new unified model for cave pearls: insights from cave pearls in Carlsbad Cavern, New Mexico, U.S.A. Journal of Sedimentary Research, 88, 344-364. doi: http://dx.doi.org/10.2110/jsr.2018.21

Meresse, F., Lagabrielle, Y., Malavieille, J., Ildefonse, B., 2012. A fossil Ocean–Continent Transition of the Mesozoic Tethys preserved in the Schistes Lustrés nappe of northern Corsica. Tectonophysics 579, 4–16. doi: https://doi.org/10.1016/j.tecto.2012.06.013.

Mithen, J.P., Sear, R.P., 2014. Computer simulation of epitaxial nucleation of a crystal on a crystalline surface. The Journal of Chemical Physics 140, 1–6. doi:10.1063/1.4866035.

Molli, G., 2008. Northern Appennine-Corsica orogenic system: an updated overview. Geological Society London (Special Edition) 298, 413–442.

Molli, G., Malavieille, J., 2011. Orogenic processes and the Corsica/Apennines geodynamic evolution: insights from Taiwan. International Journal of Earth Sciences 100, 1207–1224.

Monzawa, N., Otsuki, K., 2003. Comminution and fluidization of granular fault materials: implications for fault slip behavior. Tectonophysics 367, 127 – 143. doi:https://doi.org/10.1016/S0040-1951(03)00133-1.

Niemeijer, A., Di Toro, G., Griffith, W.A., Bistacchi, A., Smith, S.A.F., Nielsen, S., 2012. Inferring earthquake physics and chemistry using an integrated field and laboratory approach. Journal of Structural Geology 39, 2–36. doi:https://doi.org/10.1016/j.jsg.2012.02.018.

Noiriel, C., Renard, F., Doan, M.L., Gratier, J.P., 2010. Intense fracturing and fracture sealing induced by mineral growth in porous rocks. Chemical Geology 269, 197–209. doi:https://doi.org/10.1016/j.chemgeo.2009.09.018.

Oliver, N.H., Bons, P.D., 2001. Mechanisms of fluid flow and fluid–rock interaction in fossil metamorphic hydrothermal systems inferred from vein–wallrock patterns, geometry and microstructure. Geofluids 1, 137-162. doi:10.1046/j.1468-8123.2001.00013.x

Okamoto, A., Saishu, H., Hirano, N., Tsuchiya, N., 2010, Mineralogical and textural variation of silica minerals in hydrothermal flow-through experiments: Implications for quartz vein formation. Geochimica et Cosmochimica Acta 74, 3692–3706. doi:http://dx.doi.org/10.1016/j.gca.2010.03.031.

Putnis, A., Putnis, C.V., 2007. The mechanism of reequilibration of solids in the presence of a fluid phase. Journal of Solid State Chemistry 180, 1783–1786. doi:https://doi.org/10.1016/j.jssc.2007.03.023.

Reches, Z., Dewers, T.A., 2005. Gouge formation by dynamic pulverization during earthquake rupture. Earth and Planetary Science Letters 235, 361-374. doi:https://doi.org/10.1016/j.epsl.2005.04.009.

Rempe, M., Smith, S.A.F, Ferri, F., Mitchell, T.M., Di Toro, G., 2014. Clast-cortex aggregates in experimental and natural calcite-bearing fault zones. Journal of Structural Geology 68,142-157. doi: https://doi.org/10.1016/j.jsg.2014.09.007.

Rosato, A., Strandburg, K.J., Prinz, F., Swendsen, R.H., 1987. Why the Brazil nuts are on top: Size segregation of particulate matter by shaking. Physical Review Letters 58, 1038–1040. doi:10.1103/PhysRevLett.58.1038.

Rowe, C.D., Griffith, W.A., 2015. Do faults preserve a record of seismic slip: A second opinion. Journal of Structural Geology 78, 1–26. doi:https://doi.org/10.1016/j.jsg.2015.06.006.

Rowe, C.D., Kirkpatrick, J.D., Brodsky, E.E., 2012. Fault rock injections record paleo-earthquakes. Earth and Planetary Science Letters 335-336, 154–166. doi:https://doi.org/10.1016/j.epsl.2012.04.015.

Schindelin, J., Arganda-Carreras, I., Frise, E., Kaynig, V., Longair, M., Pietzsch, T., Preibisch, S., Rueden, C., Saalfeld, S., Schmid, B., Tinevez, J.Y., White, D.J., Hartenstein, V., Eliceiri, K., Tomancak, P., Cardona, A., 2012. Fiji: an open-source platform for biological-image analysis. Nature Methods 9, 676–682. doi:http://dx.doi.org/10.1038/nmeth.2019.

Scholz, C.H., 2019. The Mechanics of Earthquake and Faulting. 3rd Edition. University Press, Cambridge.

Searl, A., 1989. Saddle dolomite: a new view of its nature and origin. Mineralogical Magazine 53, 547–555. doi:10.1180/minmag.1989.053.373.05.

Sibson, R.H., 1975. Generation of Pseudotachylyte by Ancient Seismic Faulting. Geophysical Journal of the Royal Astronomical Society 43, 775–794. doi:10.1111/j.1365-246X.1975.tb06195.x.

Sibson, R.H., 1977. Fault rocks and fault mechanisms. Journal of the Geological Society 133, 191–213. doi:http://dx.doi.org/10.1144/gsjgs.133.3.0191.

Sibson, R.H., 1981. Fluid flow accompanying faulting: field evidence and models. In: Simpson, D.W., Richards, P.G. (Eds.), Earthquake Prediction: an International Review, Maurice Ewing Series, vol. 4. American Geophysical Union, pp. 897-900.

Sibson, R.H., 1985. Stopping of earthquake ruptures at dilational fault jogs. Nature 316, 248–251. doi:ttp://dx.doi.org/10.1038/316248a0.

Sibson, R.H., 1986. Brecciation processes in fault zones: Inferences from earthquake rupturing. Pure and Applied Geophysics, 159– 175. doi:10.1007/BF00875724.

Sibson, R.H., 1989. Earthquake faulting as a structural process. Journal of Structural Geology 11, 1–14. doi:https://doi.org/10.1016/0191-8141(89)90032-1.

Sibson, R.H., 1990. Conditions for fault-valve behaviour. Geological Society, London, Special Publications 54, 15–28. doi:10.1144/GSL.SP.1990.054.01.02.

Sijbers, J., Postnov, A., 2004. Reduction of ring artefacts in high resolution micro-CT reconstructions, Physics in Medicine and Biology, 49(14) N247.

Siman-Tov, S., Brodsky, E.E., 2018. Gravity-Independent Grain Size Segregation in Experimental Granular Shear Flows as a Mechanism of Layer Formation. Geophysical Research Letters 45. doi:10.1029/2018GL078486.

Smith, S.A.F., Billi, A., Di Toro, G., Spiess, R., 2011. Principal Slip Zones in Limestone: Microstructural Characterization and Implications for the Seismic Cycle (Tre Monti Fault, Central Apennines, Italy). Pure and Applied Geophysics 168, 2365–2393. doi:10.1007/s00024-011-0267-5.

Smith, S.A.F., Collettini, C., Holdsworth, R.E., 2008. Recognizing the seismic cycle along ancient faults: CO_2-induced fluidization of breccias in the footwall of a sealing low-angle normal fault. Journal of Structural Geology 30, 1034–1046. doi:https://doi.org/10.1016/j.jsg.2008.04.010.

Snoke, A.W., Tullis, J., Todd, V.R., 1998. Fault-related Rocks: A Photographic Atlas. Princeton University Press, Princeton, New Jersey.

Spry, A., 1969. Metamorphic Textures. Pergamon Press, Oxford, London, Edinburgh, New York, etc.

Taber, S., 1916. The Growth of Crystals Under External Pressure. American Journal of Science 41, 532–556. doi:10.2475/ajs.s4-41.246.532.

Taresewicz, J.P.T., Woodcock, N.H., Dickson, J.A.D., 2005. Carbonate dilation breccias: examples from the damage zone to the Dent Fault, northwest England. Geological Society of America Bulletin, 117, 736-745.

Tenthorey, E., Cox, S F., Todd, H F., 2003. Evolution of strength recovery and permeability during fluid-rock reaction in experimental fault zones. Earth and Planetary Science Letters, 206, 161–172. doi:http://dx.doi.org/10.1016/S0012-821X(02)01082-8.

Turcotte, D.L., 1986. Fractals and fragmentation. Journal of Geophysical Research: Solid Earth 91, 1921–1926. doi:10.1029/JB091iB02p01921.

Vitale Brovarone, A., Beyssac, O., Malavieille, J., Molli, G., Beltrando, M., Compagnoni, R., 2013. Stacking and metamorphism of continuous segments of subducted lithosphere in a high-pressure wedge: The example of Alpine Corsica (France). Earth-Science Reviews 116, 35–56. doi: https://doi.org/10.1016/j.earscirev.2012.10.003.

von Hagke, C., Kettermann, M., Bitsch, N., Bücken, D., Weismüller, C., Urai, J.L., 2019. The Effect of Obliquity of Slip in Normal Faults on Distribution of Open Fractures. Frontiers in Earth Science 7, 18. doi:10.3389/feart.2019.00018.

Walker, R.J., Holdsworth, R.E., Imber, J., Ellis, D., 2011. The development of cavities and clastic infills along fault-related fractures in Tertiary basalts on the NE Atlantic margin. Journal of Structural Geology 33, 92–106. doi:https://doi.org/10.1016/j.jsg.2010.12.001.

Warren, J., 2000. Dolomite: occurrence, evolution and economically important associations. Earth-Science reviews 52, 1-81. doi:https://doi.org/10.1016/S0012-8252(00)00022-2.

Wen, C. Y., Yu, Y. H., 1966. A generalised method for predicting minimum fluidization velocity: American Institute of Chemical Engineering Journal, May 1966, p. 610–612. doi:http://dx.doi.org/10.1002/aic.690120343.

Weyl, P.K., 1959. Pressure solution and the force of crystallization - a phenomenological theory. Journal of Geophysical Research 64, 2001-2005.

Williams, J.C., 1976. The segregation of particulate materials. a review. Powder Technology 15, 245-251. doi:https://doi.org/10.1016/0032-5910(76)80053-8.

Wiltschko, D. V., Morse, J.W., 2001. Crystallization pressure versus “crack seal” ad the mechanism for banded veins, Geology 29, 79-82.

Woodcock, N.H., Miller, A.V.M., Woodhouse, C.D., 2014. Chaotic breccia zones on the Pembroke Peninsula, South Wales: collapse into voids along dilational faults. Journal of Structural Geology 69, 91-107. doi:https://doi.org/10.1016/j.jsg.2014.09.019.

Woodcock, N.H., Mort, K., 2008. Classification of fault breccias and related fault rocks. Geological Magazine 145, 435–440. doi:10.1017/S0016756808004883.

Zheng, X., Cordonnier, B., Zhu, W., Renard, F., Jamtveit, B., 2018. Effects of confinement on reaction-induced fracturing during hydration of periclase. Geochemistry, Geophysics, Geosystems, 19, 2661–2672. doi:https://doi.org/10.1029/2017GC007322.

Zheng, X., Cordonnier, B., McBeck, J., Boller, E., Jamtveit, B., Zhu, W., Renard, F., 2019. Mixed-mode strain localization generated by hydration reaction at crustal conditions. Journal of Geophysical Research: Solid Earth, 124. doi:https://doi.org/10.1029/2018JB017008.

Figure Captions

Fig. 1. Geological setting of the Col de Teghime area (Alpine Corsica). (a) Simplified geological map with main stops (1 to 4) and orientation of points of view of Figs. 2-3. Modified from Faure and Malavieille (1981), and Dallan and Puccinelli (1995). (b) Stereonets of the orientations and lineations of faults collected at each stop. The fault planes are in black color and the average attitude of the main fault is in red color. Arrows indicate the direction of movement of the hanging wall.

Fig. 2. Faults and fault zone rocks at Stop 1. (a) Panoramic view of the outcrop (top) and sketch with lithologies, main fault rock domains, and localities of the collected samples (bottom). (b) The transition between the fault core and the damage zone is marked by sharp boundaries (dashed white line). The fault core is easily recognizable because of the reddish- to orange-color matrix that supports breccias. Dashed black lines define the metamorphic foliation. Cover lens for scale. (c) Cockade-bearing faults with inverse grading distribution of the cm-size clasts. Core clasts are surrounded by mm-thick rims of dolomite, calcite, goethite and anatase forming cockade-like texture. The upper part of the cockade-bearing vein is locally sealed by carbonate cement (Cc). Faults veins cut the cockade-bearing veins (green in color arrows indicate shear sense). Late carbonate-bearing veins (LCV) cut the entire fault core. Coin for scale. (d) Well-developed inverse grading within the cockade-bearing vein. Injection-like veins are visible intruding the footwall (white arrows). (e) Cavities (i.e.= voids not filled by cement) up to 10s of centimeters in size are only partly filled with white in color calcite crystals within the cockade-bearing faults. Sample CC05-17. (f) Minor brittle normal dip-slip fault cutting the marbles in the hanging wall. This fault accommodates normal dip-slip displacement up to 40 cm.

Fig. 3. Faults and fault zone rocks at Stop 2. (a) Fault surface of the NW-SE trending main fault marked by calcite slickenlines cutting the marbles. The field photo was taken looking the fault surface upwards. (b) Well-developed calcite slickenlines on the fault surface of the NW-SE trending main fault with marbles in hanging wall. Compass for scale. (c-d) Zoom on cockade-bearing faults showing

fault breccias with fragments surrounded by mm-think reddish rims forming cockade-like texture cemented by white in color calcite. Yellow in color arrows indicate the cockade breccias in (c). The cockade breccias are cut by mirror-like slip surfaces. White in color arrows indicate truncated cockades of the cockade-bearing vein. White in color calcite-built concretion (Cc) due to very late stage karst process within the fault zone in (c). Coin for scale.

Fig. 4. Cockade-bearing faults. (a) Key-type polished sample (sample CC01-12) with multiple cockade-bearing veins and inverse grading. (b) Sketch of the sequence of faulting and veining events. See main text for description.

Fig. 5. Cockade breccias (sample CC01-12). (a) Core clast partly contoured by the dashed white-colored line and surrounded by the four concentric rims of (from the core clast outwards): (1) saddle dolomite enriched in Ca and Fe; (2) Mg-calcite with goethite and anatase microcrystals; (3) zoned saddle dolomite; (4) Mg-calcite with goethite and anatase microcrystals. The cavities between the cockades are filled by calcian dolomite "sealing cement" and late stage pure calcite (V8). (b) Elaborated EDX map showing the spatial distribution of mineral phases in the cockade breccia. (c) Under the optical microscope (OM) in parallel-polarized light (PPL), the dolomite-built rims are transparent, while the hydroxide- and oxide-rich rims are brownish in color. (d) OM cathodoluminescence (OM-CL) images of the same area as in (c): the CL signal for dolomite is mostly "quenched"; while, for calcite it indicates strong chemical zoning. (e) OM-CL image of cockade breccia showing the carbonate-built rims surrounding entirely the core clasts made of the quartzite host rock. The dashed white-colored lines mark the core clasts. (f) Acicular- and spherulitic-shaped crystals of goethite (Gt) and anatase (Ant) partly filling the micropores parallel to the calcite habit.

Fig. 6. Microstructures of the cockade-bearing faults. (a) High-resolution scan of a cockade-bearing vein which does not have inverse grading within the slipping zone (sample CC11-17). The cockade-

bearing vein is bordered by slipping surfaces. The core clasts do not show any preferential orientation within the slipping zone. Dashed red-color box marks the zoom in (b). (b) Zoom on the slipping zone (photomosaic of BSE images). The core clasts are made of both quartzite and reworked-vein fragments and are wrapped by carbonate-built rims, forming cockade-like texture. The cockades are sealed by a dolomite in composition cement. Pores are black in color in BSE image. (c) Core clast made of cataclastic to ultracataclastic quartzite (cross-polarized light micrograph from sample CC01-12). The cockade rims separate the core clasts and, when cockades are in contact with the adjacent ones, they form triple junctions.

Fig. 7. Slipping zones of cockade-bearing faults at Stop 2. (a) Scan of the thin section of sample CB04-07. The cockade-bearing vein is cut by multiple mirror-like slip surfaces, which truncate the cockades. The cockade-bearing vein cuts a slipping zone filled with cortex-clasts aggregates (CCAs). Below the CCAs-bearing slip zone, multiple slip surfaces and zones are recognized. Slip zones consist of protobreccias and cataclasites. Dashed yellow-colored boxes indicate the zooms in (b-e). (b-c) Parallel-polarized light micrographs of the cockades. The core clasts consist of fragments of the marble-built host rock wrapped by carbonate-built rims with opaque minerals. The cockade rims appear "dusty" because of the opaque minerals (goethite from XRPD analysis). The cockades are sealed by white in color calcite cement and, locally, form triple junctions, when they are in contact with the adjacent ones as shown in (c). (d-e) Parallel-polarized light micrographs of the CCAs similar to those experimentally produced by Rempe et al. (2014). The CCAs consist of marble fragments, calcite and opaque minerals.

Fig. 8. Microstructures of the faulting and veining events in the cockade-bearing faults (sample CC01-12). (a) Dolomite-rich vein V7 cuts and intrudes the brownish ultracataclastic fault vein V4 and the cockade-bearing vein V3. (b) Cockade-bearing vein (V3) cut by fault vein V4. The latter is made of fine angular quartzite fragments sealed by calcian dolomite. (c) Zoom on the matrix of V4

made of calcian dolomite, goethite and anatase. (d) OM-CL image of a cavity (V8) filled by pure calcite with strong chemical zoning. OM-PPL image of (d) on the top right corner.

Fig. 9. Cumulative clast size distributions (CSDs) of the (1) cores (i.e.= core clasts) of the cockade breccia with inverse grading (V3, sample CC01-12), (2) cores of the cockade breccia without inverse grading (sample CC11-17), (3) clasts of the fine grained cataclastic fault vein (V4, sample CC01-12) and, for comparison, (4) clasts in similar dolomite-bearing fault veins from strike-slip faults cutting dolostones (Fondriest et al., 2012; green in color curve). The CSDs in the cockade-bearing faults and from the dolomite-bearing fault veins described by Fondriest et al. (2012) are compatible with a process of elutriation of clasts smaller than 300 μm in diameter due to co-seismic fluidization. The elutriated smaller clasts are thought to form the ultrafine cataclastic fault veins (V4, see also the conceptual model discussed in Fig. 11). Clasts were drawn by hand and their distribution determined with the software Fiji (Schindelin et al., 2012) as discussed in section 3. The thick vertical gray in color line at a clast size of ~310 μm marks the abrupt change in slope of the CSD for the cockade-bearing veins due to the lack of fine particles. The dashed black segments are the slopes of the CSDs before their abrupt change in slope.

Fig. 10. 3-Dimensional reconstructions based on micro-CT analysis of the cockade-bearing fault in three volumes throughout the cockade-bearing vein (V3) with inverse grading (sample CC01-12). Core clasts do not touch each other and are separated apart by carbonate-built rims. (a) The darkest grey levels are given by quartzite-built clasts and by the presence of open cavities. (b) Fine angular clast-supported fault vein (V4) cuts the cockade-bearing vein (V3). (c) The smallest cockades are found towards the footwall.

Fig. 11. Conceptual model of the formation of cockade-bearing faults (right column) and its relationship to fault displacement and time during the seismic cycle (left column). (a) Co-seismic

fragmentation: earthquake rupture propagation along a fluid-rich fault and consequent fragmentation and implosion of the wall rocks. (b) Zoom on fault dilatant site: co-seismic fluidization due to ingression of CO_2- and Fe-rich fluids promotes (1) collision, abrasion, comminution of wall rock fragments; (2) sorting and elutriation of finer clasts (see Fig. 12a); (3) inverse grading associated with shacking (Brazil-Nut Effect) and shearing (see Fig. 12b-c). (c) Post-seismic fault sealing: formation of cockades due to precipitation of saddle dolomite + Mg-calcite + goethite + anatase by pressure-growth mechanism at fault dilatant sites, which are relatively unloaded compared to the rest of the fault. The formation of cockade rims results in the progressive separation of the core clasts. Pressure growth preserves the clast arrangement (inverse grading) resulted from the sorting of the fluidized granular material during seismic slip. The finer elutriated clasts will form the distal parts of the fluidized material (see also the fault veins V4 in Fig. 4).

Fig. 12. Physical processes promoting clast size selection and inverse grading. (a) Modeled relationships between superficial flow velocity and particle diameters for minimum fluidization (blue-color curve; u_m) and entrained flow regime (orange-color curve; u_t) for spherical particles. The vertical dashed black line indicates the cut-off value of 310 μm in diameter observed in the cockade-bearing veins (Fig. 9). As a result, a superficial flow velocity of 0.13 m/s is required to elutriate clasts ≤ 310 μm in size. According to this model, at the superficial velocity of 0.13 m/s clasts ≤ 2.3 cm in diameter can be fluidized (i.e., float in the flow; see horizontal dashed black line in the upper diagram). See the text for the boundary conditions assumed for the modeling. (b) Brazil-Nut Effect: sequences of shaking of a 50/50 binary mixture with size ratio 1:5 from the initial random placement to the configuration (i.e.= inverse grading) obtained after 300 shakes. Seismic shaking is expected to yield similar effects on granular materials (modified from Rosato et al., 1987). (c) Simple shear of particles of different size leads to downward motion of the smaller ones (passing through the voids) and formation of inverse grading.

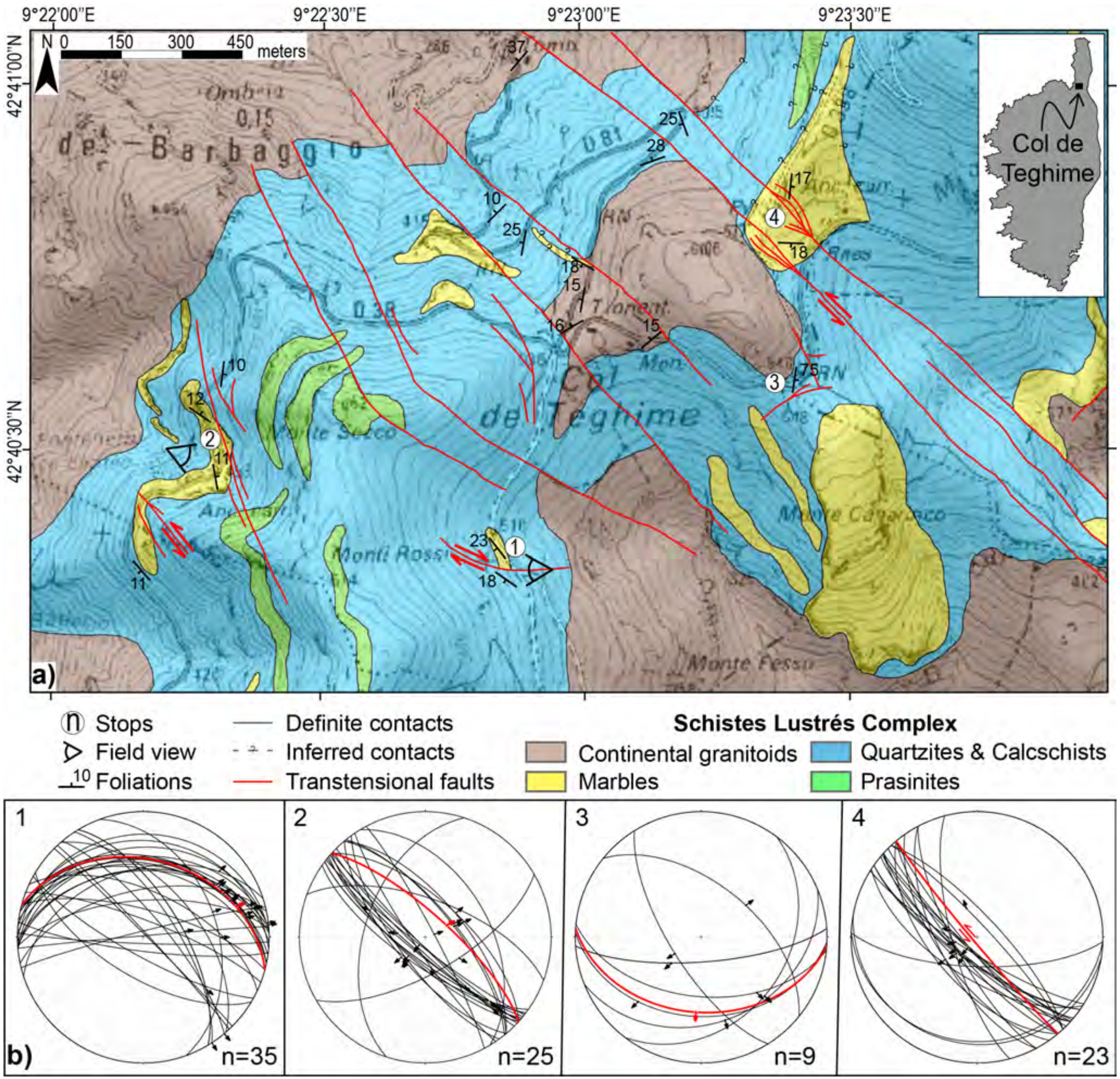
9°22'00''E
9°22'30''E
9°23'00''E
9°23'30''E
42°41'00''N
42°40'30''N
N
0 150 300 450 meters
Col de Teghime
de Barbaggio
Col de Teghime
Monti Rossi
Monte Canarinco
Monte Fesso
a)
Stops
Field view
Foliations
Definite contacts
Inferred contacts
Transtensional faults
Schistes Lustrés Complex
Continental granitoids
Marbles
Quartzites & Calcschists
Prasinites
b)
1
n=35
2
n=25
3
n=9
4
n=23

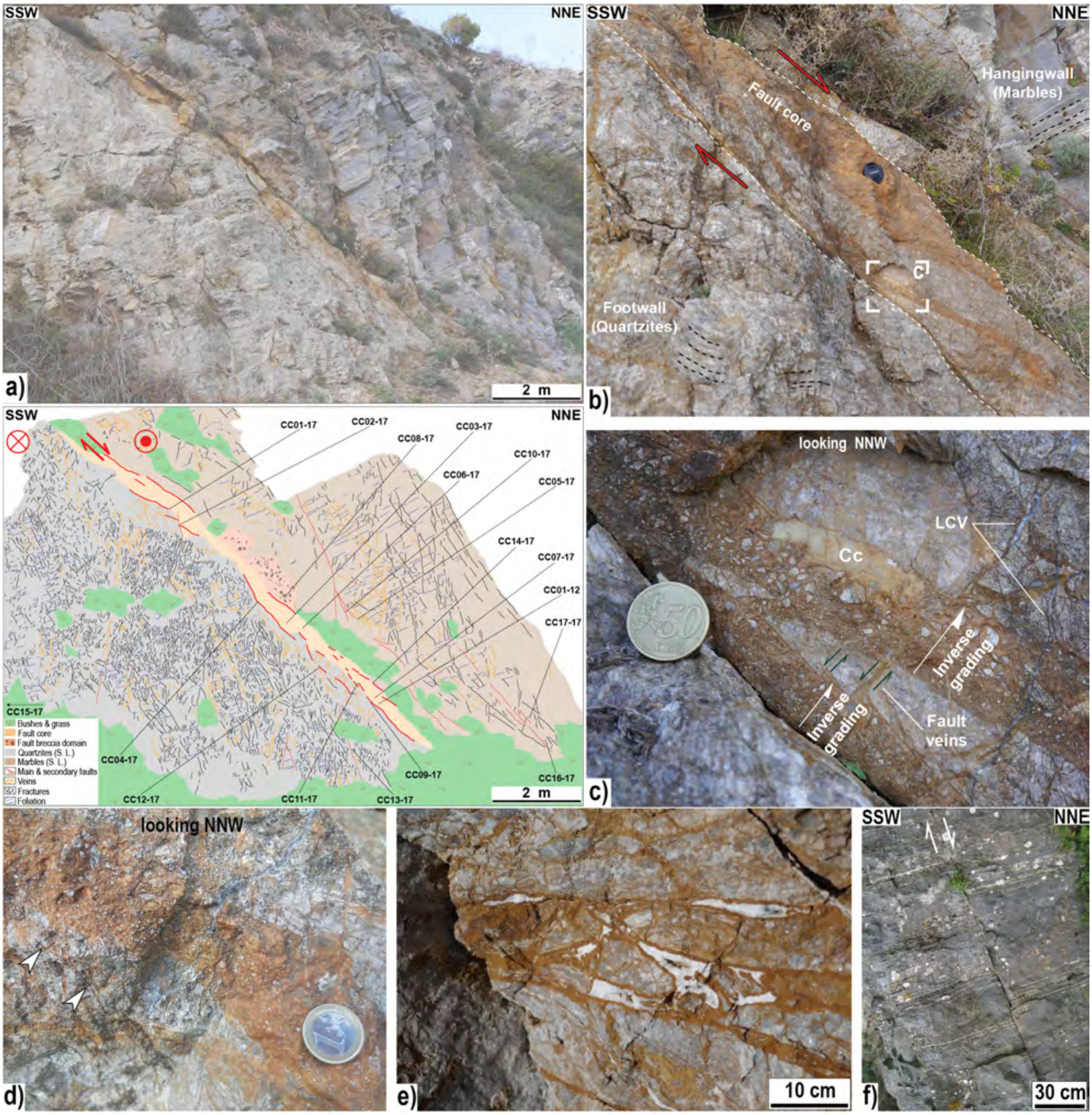
SSW
NNE
a)
2 m
SSW
NNE
Hangingwall
(Marbles)
Fault core
Footwall
(Quartzites)
c
b)
SSW
NNE
CC01-17
CC02-17
CC08-17
CC03-17
CC10-17
CC06-17
CC05-17
CC14-17
CC07-17
CC01-12
CC17-17
CC15-17
CC04-17
CC12-17
CC11-17
CC13-17
CC09-17
CC16-17
Bushes & grass
Fault core
Fault breccia domain
Quartzites (S. L.)
Marbles (S. L.)
Main & secondary faults
Veins
Fractures
Foliation
2 m
looking NNW
LCV
Cc
Inverse grading
Inverse grading
Fault veins
c)
looking NNW
d)
e)
10 cm
SSW
NNE
f)
30 cm

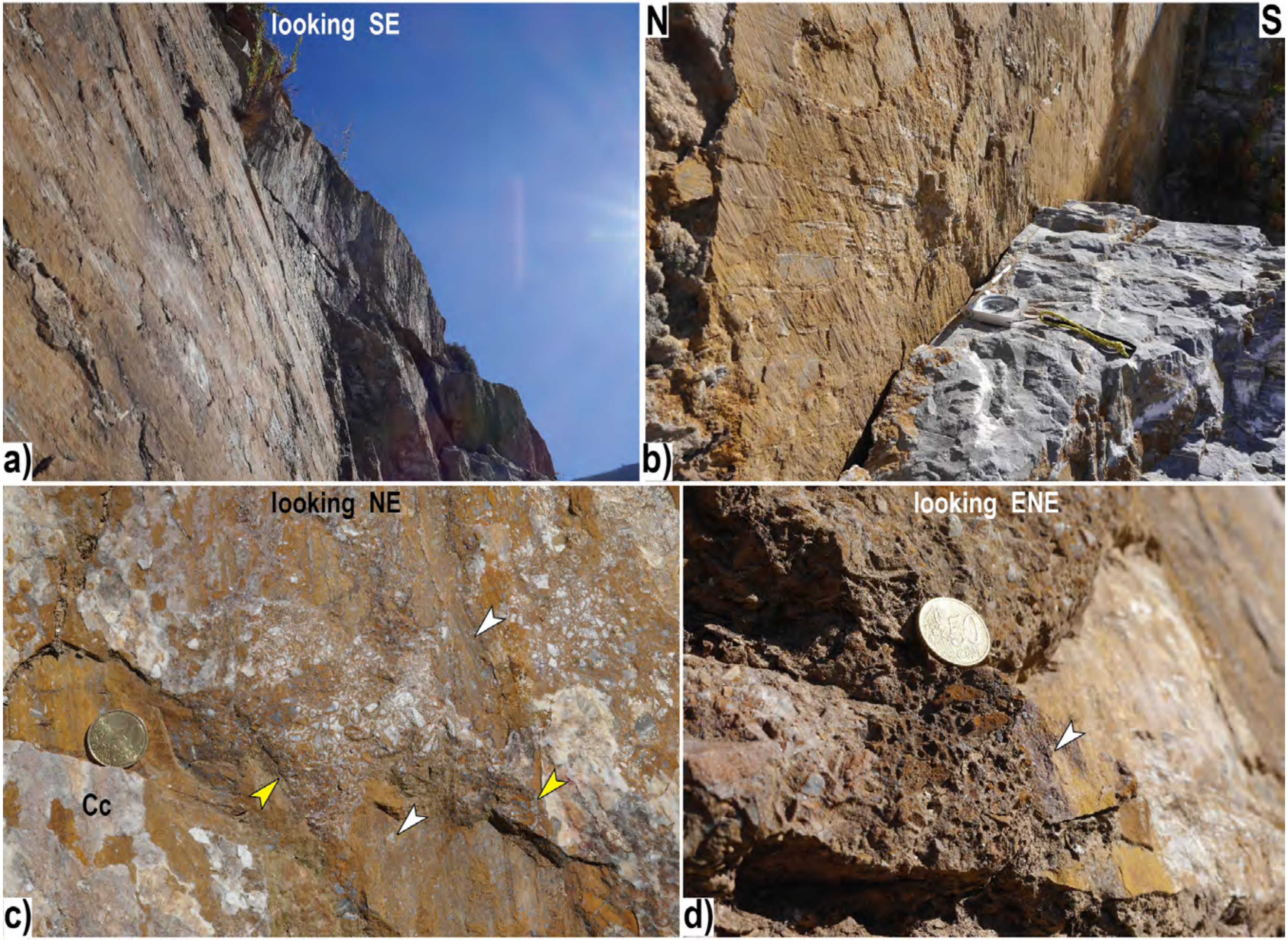
looking SE
a)
N
S
b)
looking NE
Cc
c)
looking ENE
d)

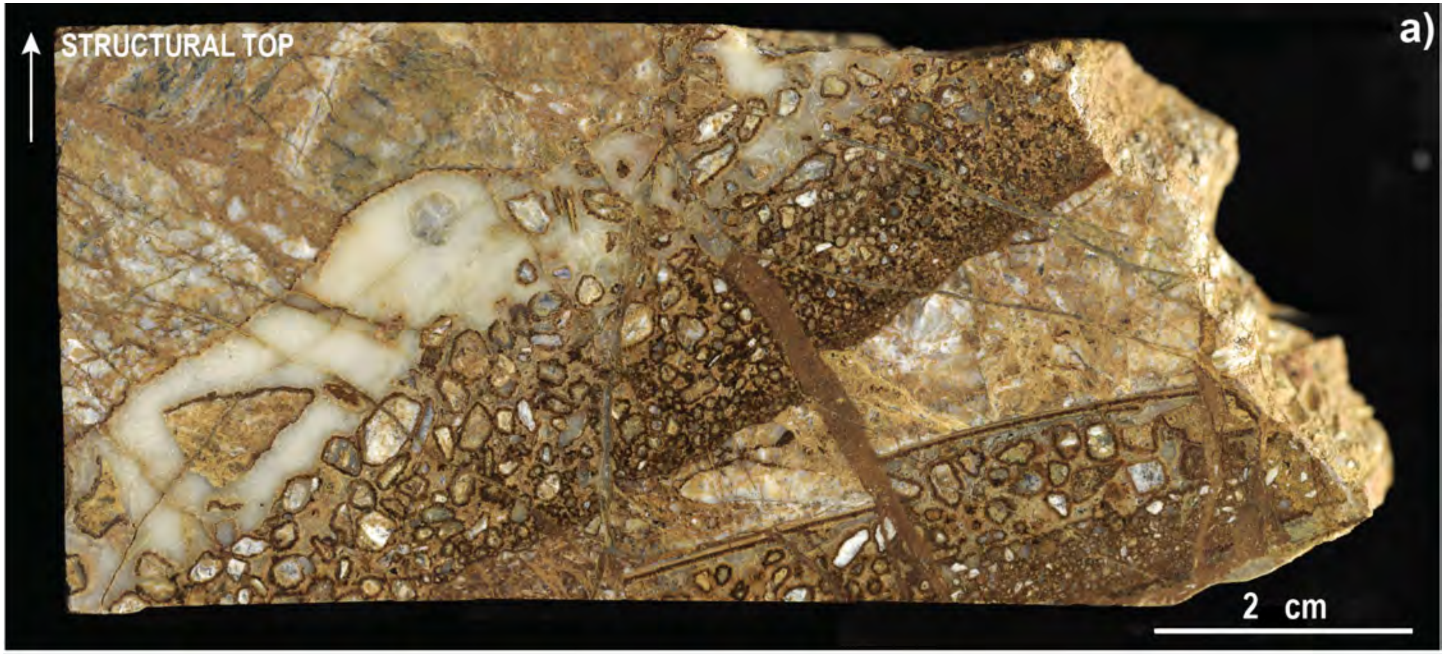
STRUCTURAL TOP
a)
2 cm

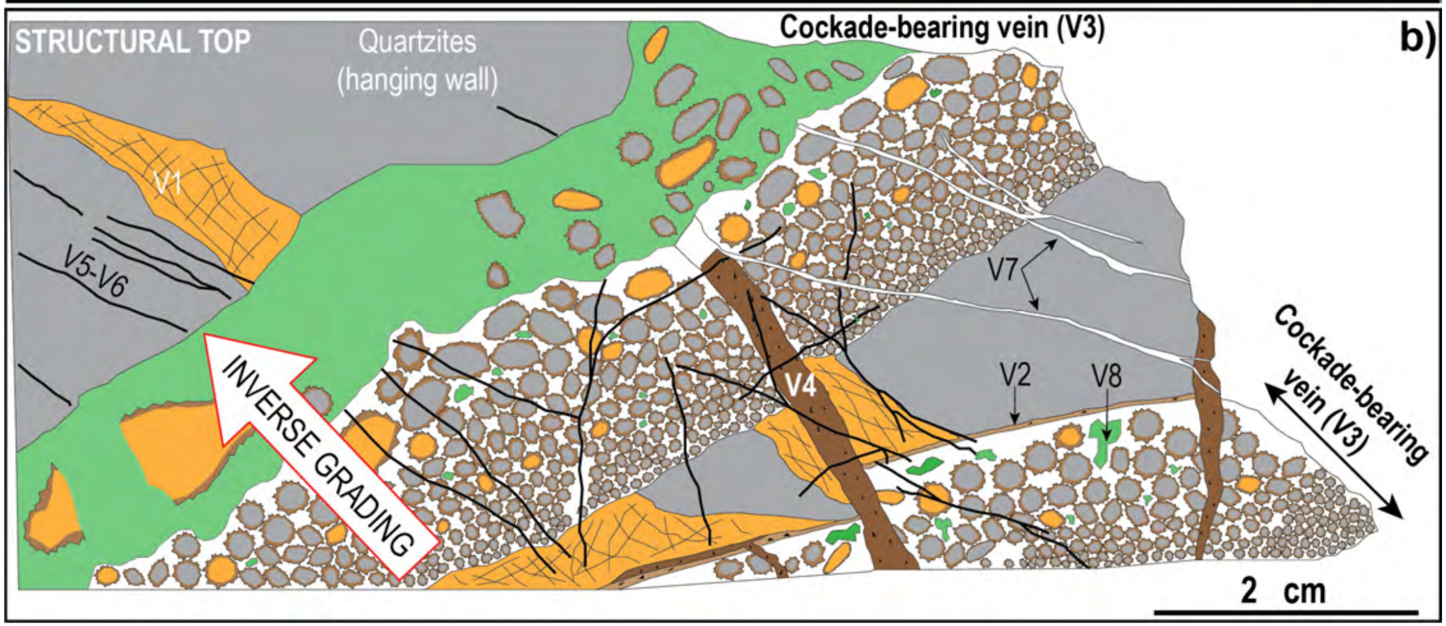
STRUCTURAL TOP
Quartzites
(hanging wall)
Cockade-bearing vein (V3)
b)
V1
V5-V6
INVERSE GRADING
V7
V4
V2
V8
Cockade-bearing vein (V3)
2 cm

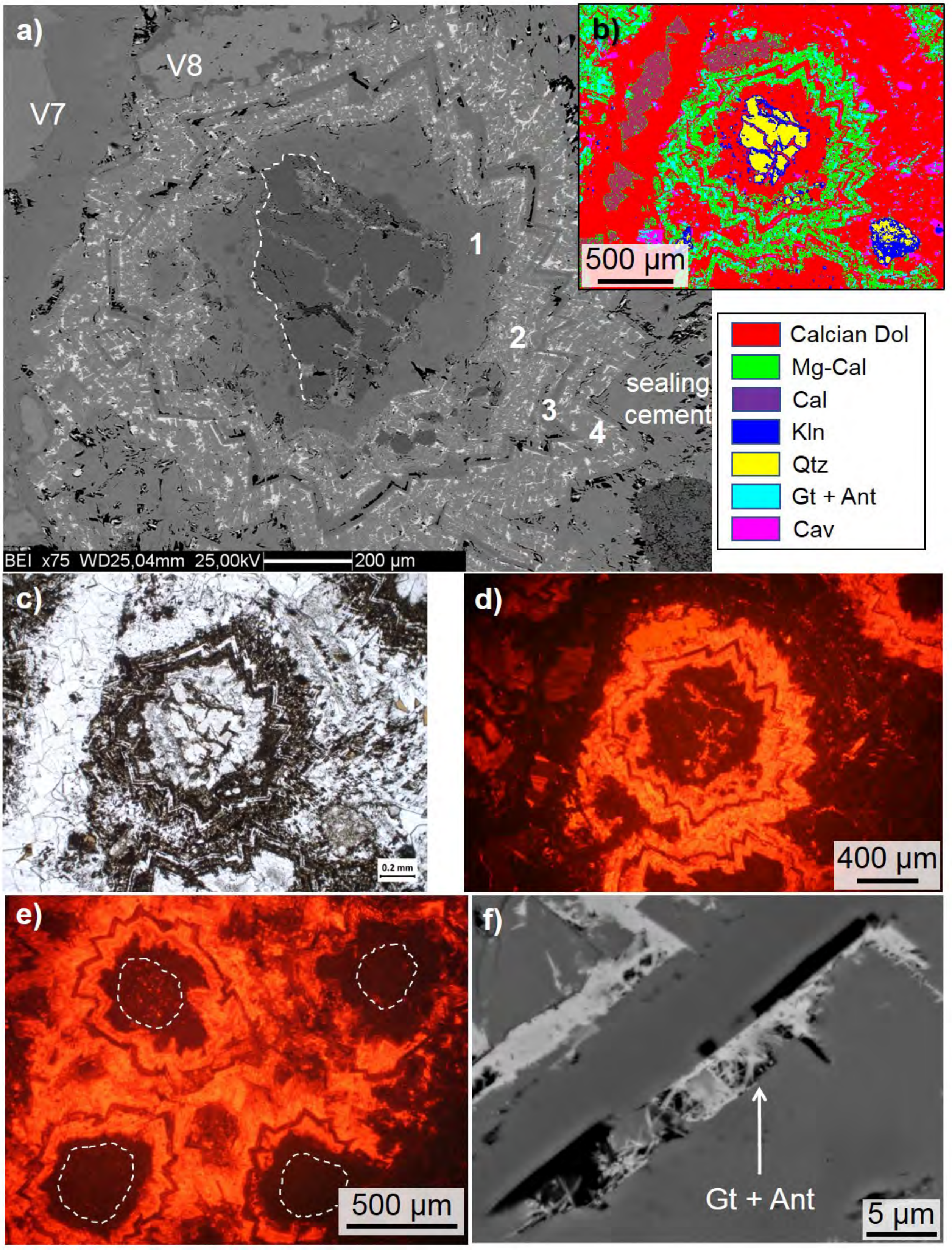

a)
V8
V7
1
2
3
4
sealing cement
BEI x75 WD25,04mm 25,00kV 200 µm
b)
500 µm
Calcian Dol
Mg-Cal
Cal
Kln
Qtz
Gt + Ant
Cav
c)
0.2 mm
d)
400 µm
e)
500 µm
f)
Gt + Ant
5 µm

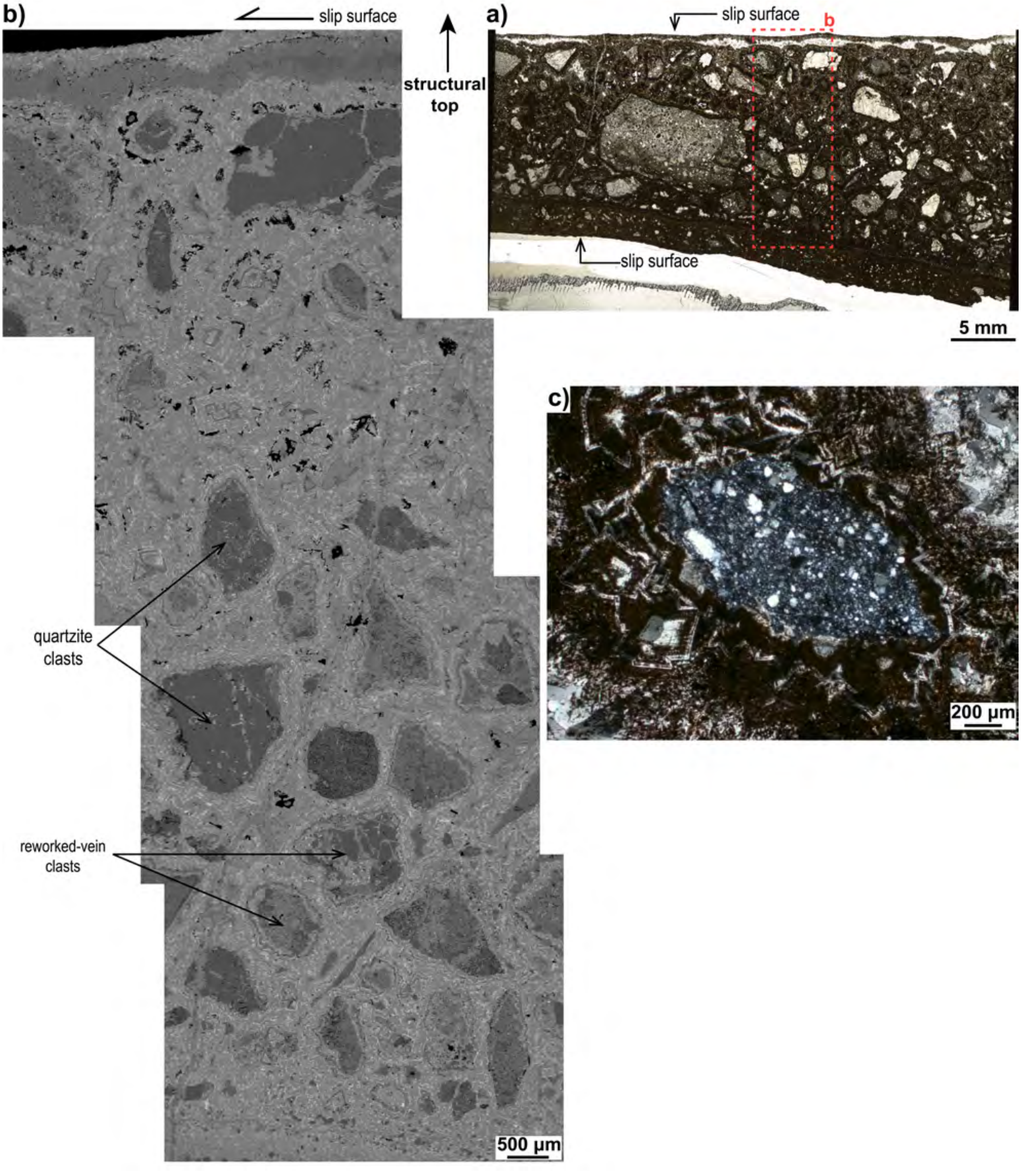
b)
slip surface
structural top
a)
slip surface
b
slip surface
5 mm
c)
200 µm
quartzite clasts
reworked-vein clasts
500 µm

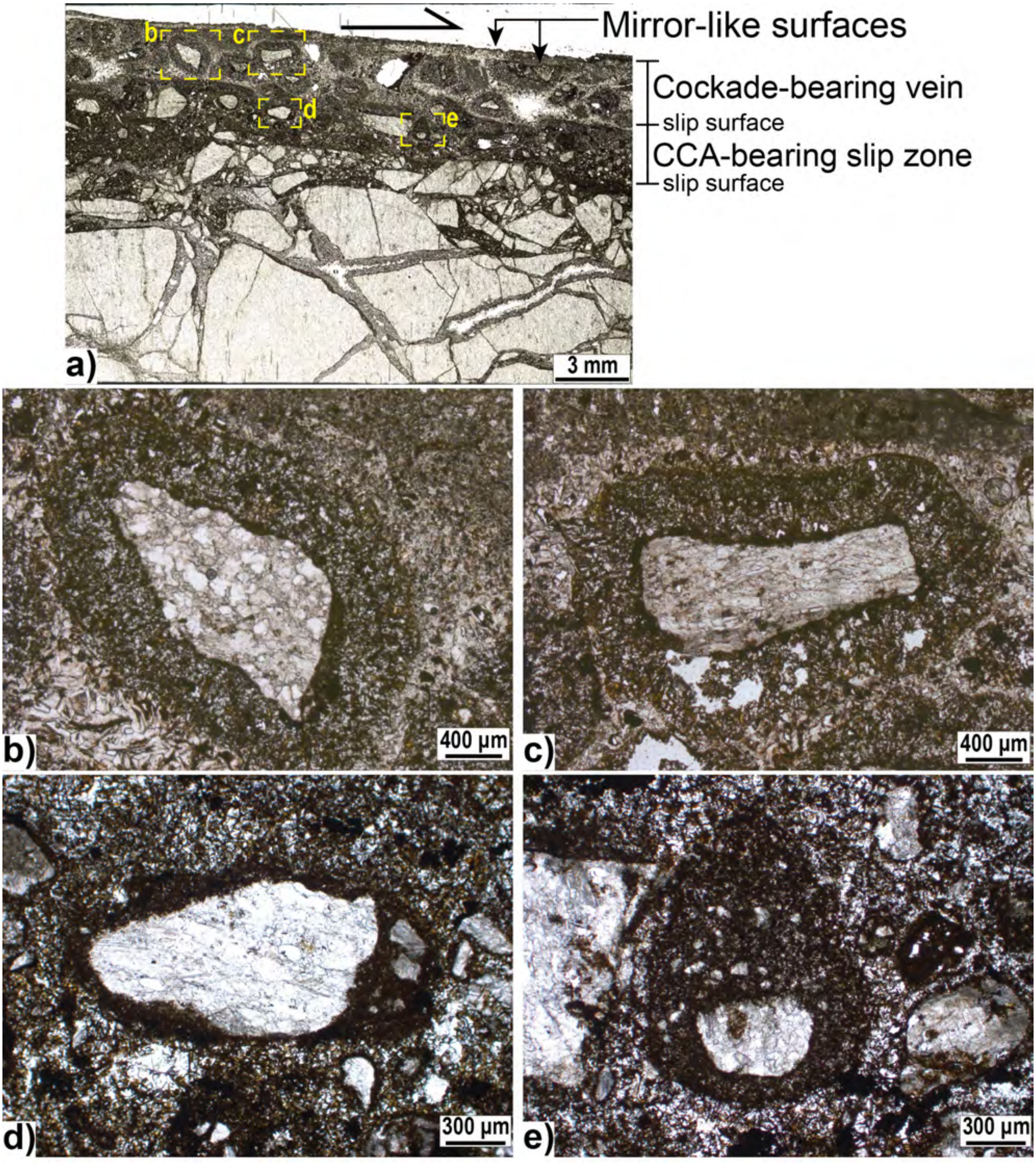

Mirror-like surfaces
Cockade-bearing vein
slip surface
CCA-bearing slip zone
slip surface
b
c
d
e
a)
3 mm
b)
400 µm
c)
400 µm
d)
300 µm
e)
300 µm

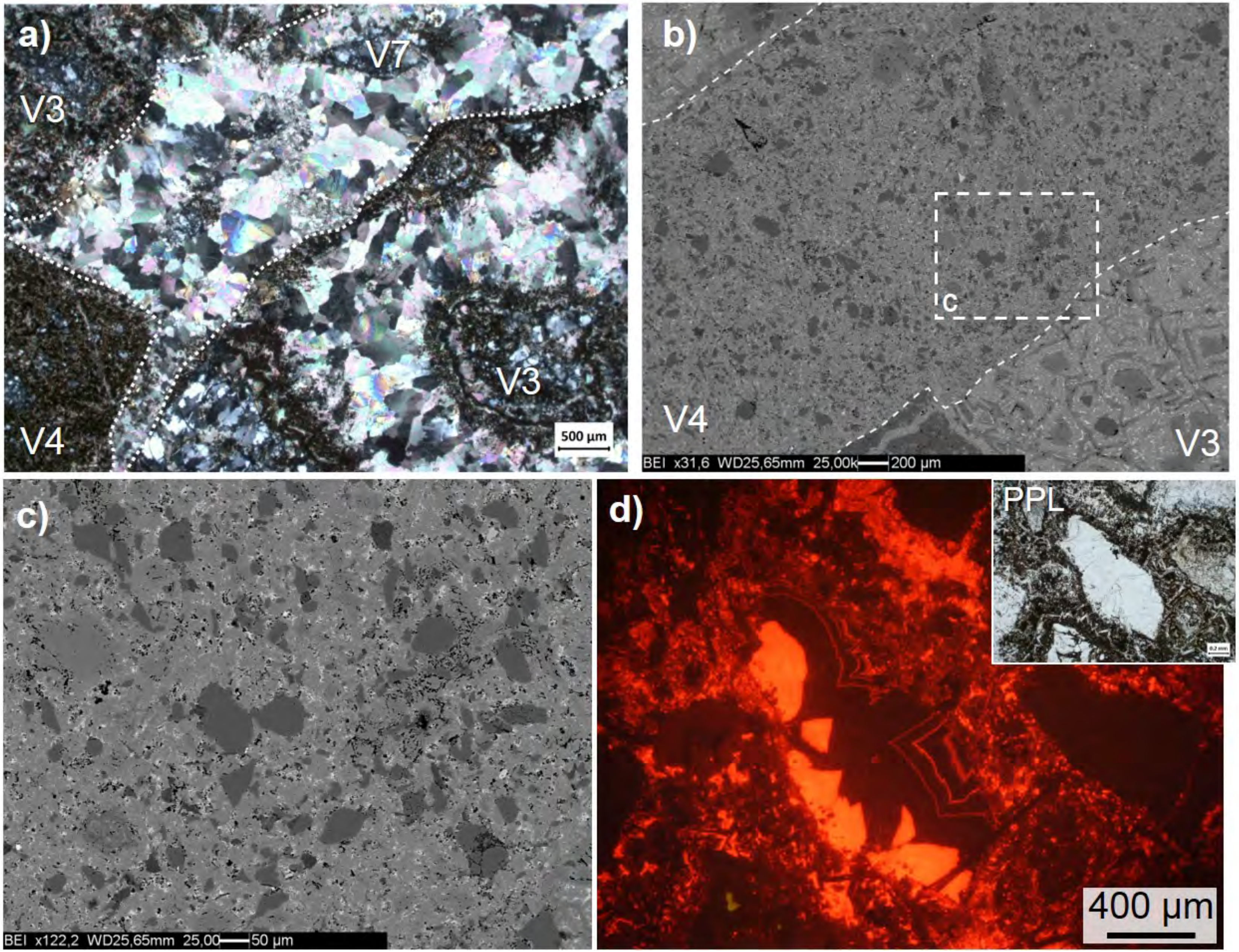
a)
V7
V3
V3
V4
500 µm
b)
c
V4
V3
BEI x31,6 WD25,65mm 25,00kV 200 µm
c)
BEI x122,2 WD25,65mm 25,00 50 µm
d)
PPL
400 µm

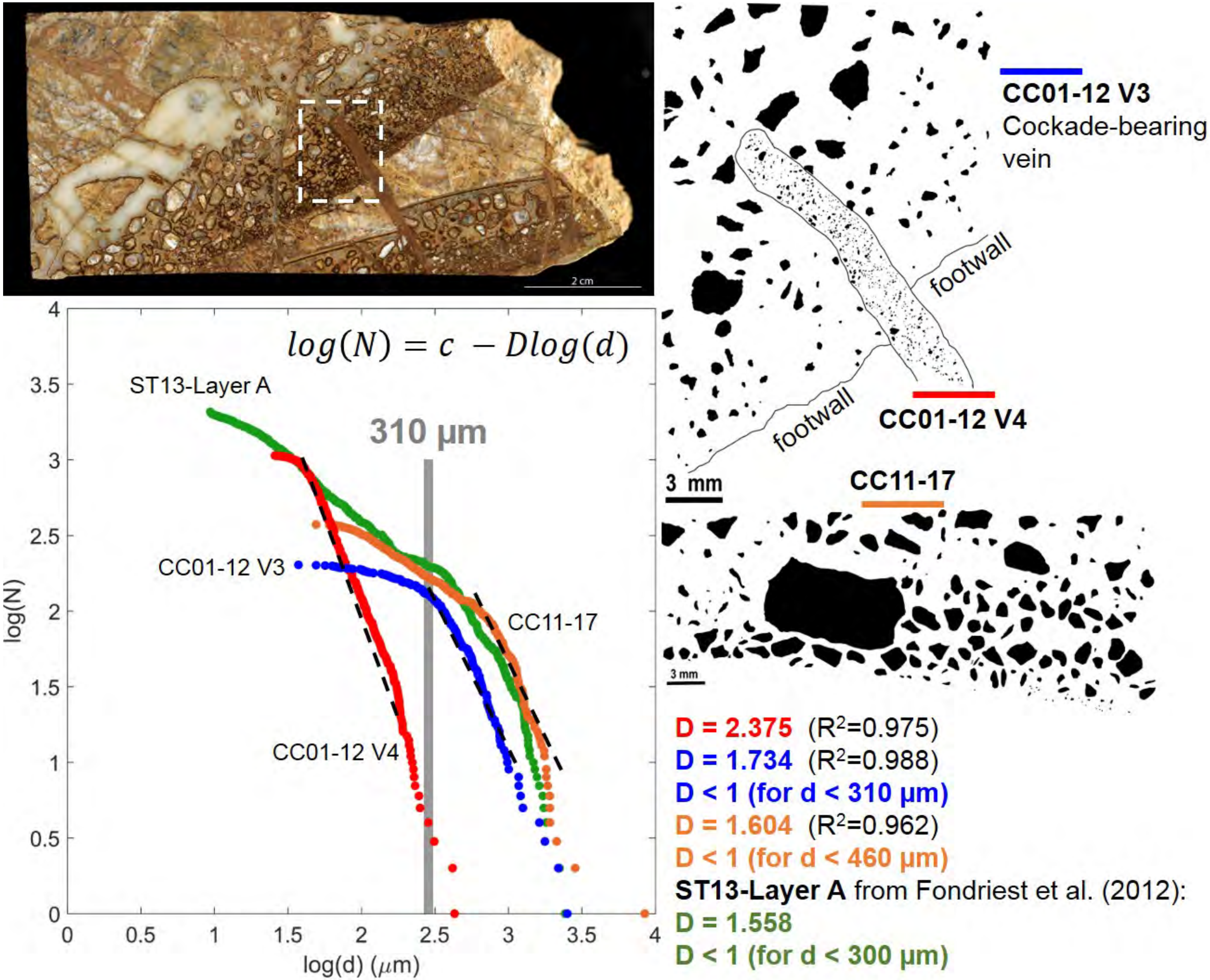

2 cm
$log(N) = c - Dlog(d)$
ST13-Layer A
310 µm
CC01-12 V3
CC11-17
CC01-12 V4
log(N)
log(d) (µm)
CC01-12 V3
Cockade-bearing
vein
footwall
footwall
CC01-12 V4
3 mm
CC11-17
3 mm
D = 2.375 (R^2=0.975)
D = 1.734 (R^2=0.988)
D < 1 (for d < 310 µm)
D = 1.604 (R^2=0.962)
D < 1 (for d < 460 µm)
ST13-Layer A from Fondriest et al. (2012):
D = 1.558
D < 1 (for d < 300 µm)

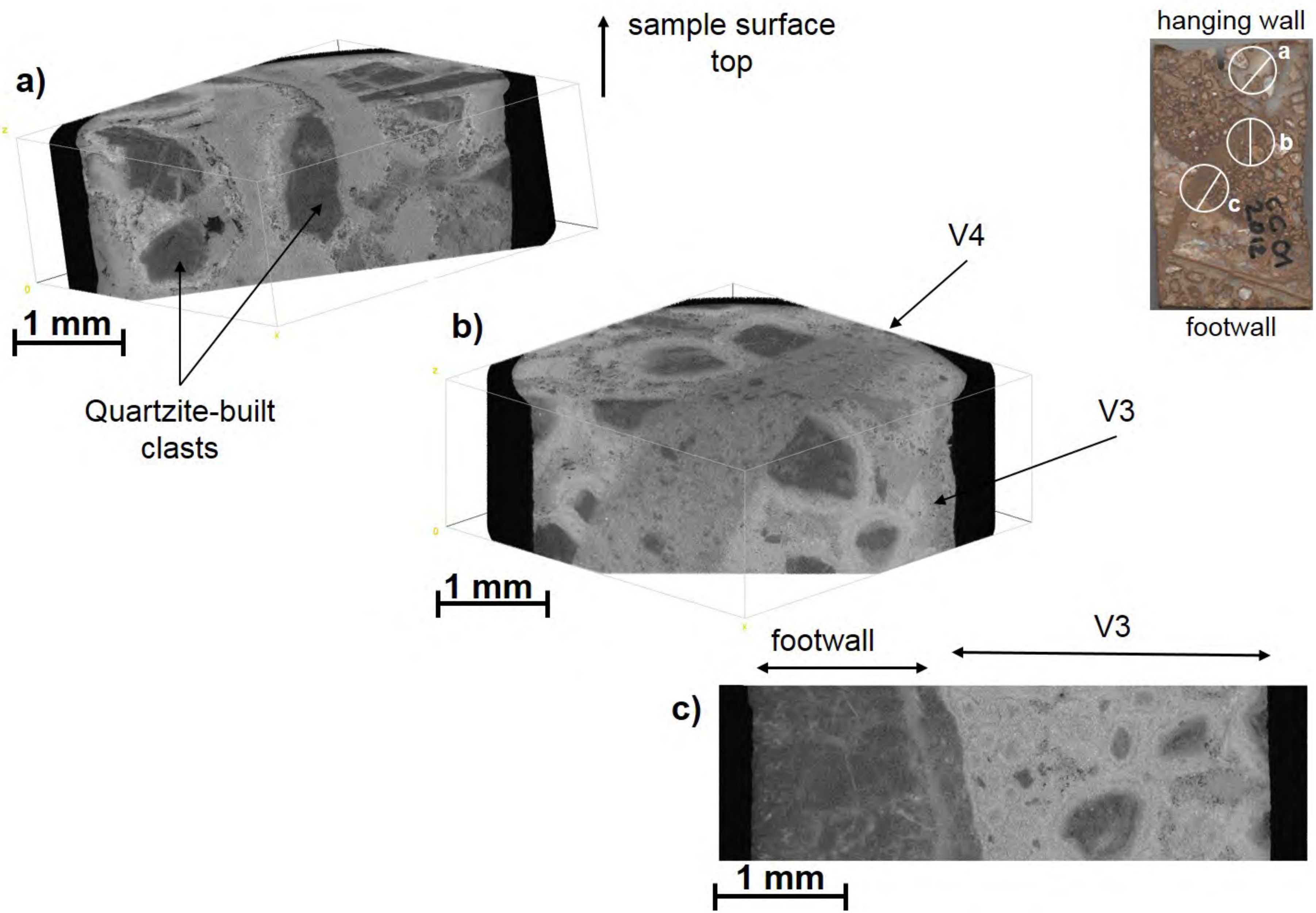

sample surface
top
hanging wall
a
b
c
footwall
a)
1 mm
Quartzite-built
clasts
b)
V4
V3
1 mm
footwall
V3
c)
1 mm

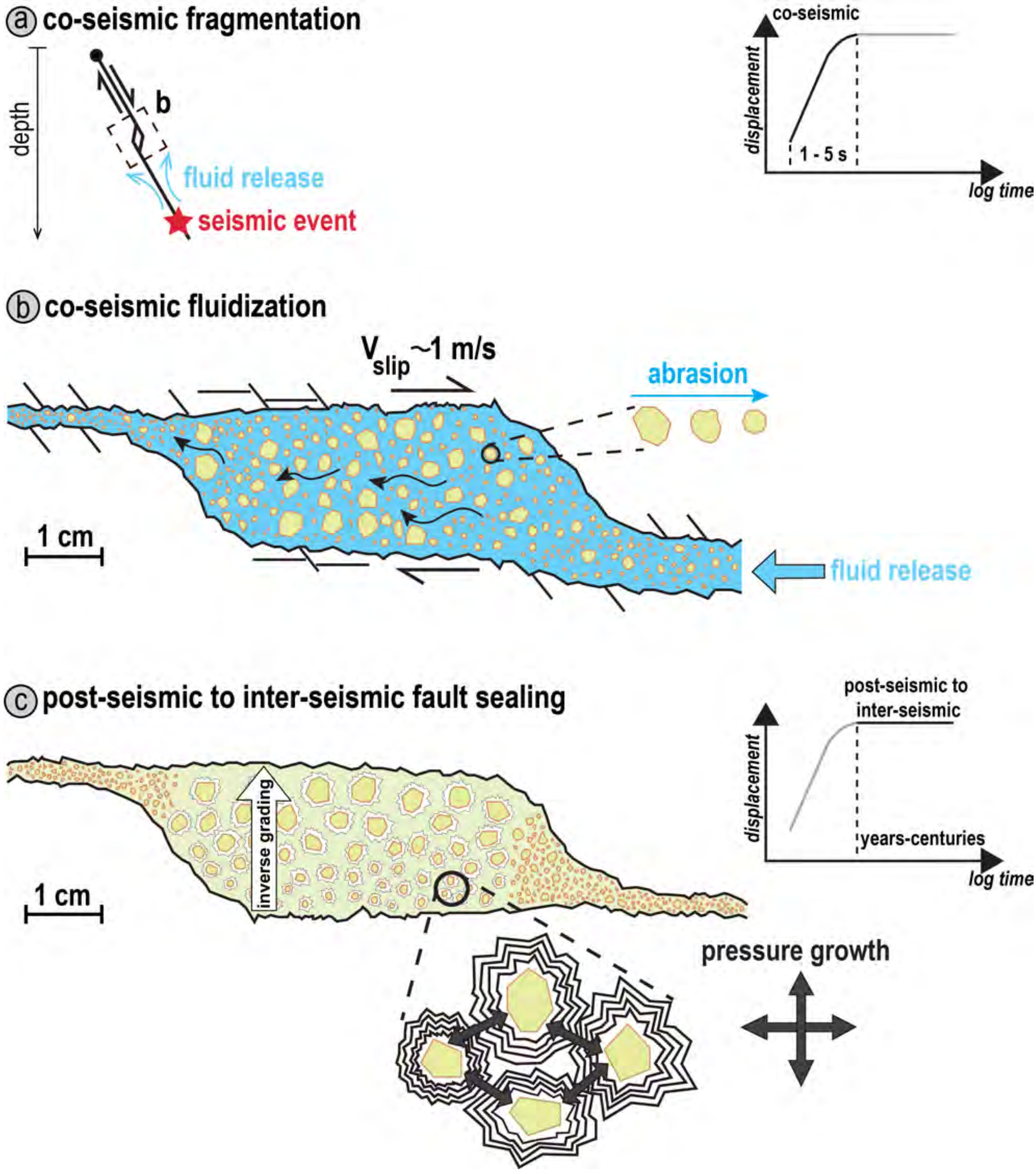
a co-seismic fragmentation
depth
b
fluid release
seismic event
co-seismic
displacement
1 - 5 s
log time
b co-seismic fluidization
V slip ~1 m/s
abrasion
1 cm
fluid release
c post-seismic to inter-seismic fault sealing
inverse grading
1 cm
post-seismic to
inter-seismic
displacement
years-centuries
log time
pressure growth

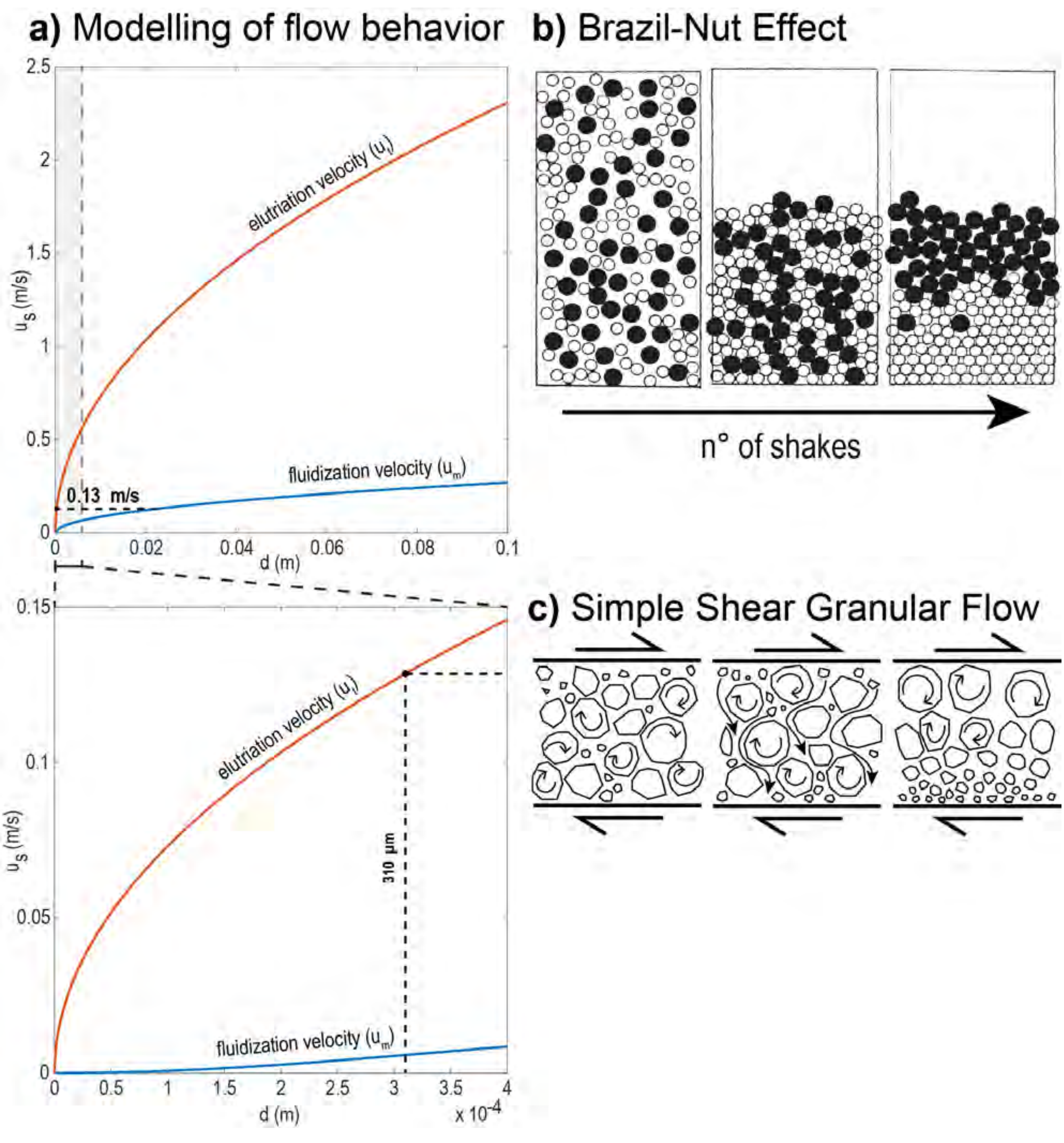

a) Modelling of flow behavior
b) Brazil-Nut Effect
c) Simple Shear Granular Flow
elutriation velocity (u_t)
fluidization velocity (u_m)
0.13 m/s
u_S (m/s)
d (m)
310 μm
x 10^{-4}
n° of shakes